Systems/Circuits

Postnatal Maturation of Membrane Potential Dynamics during *in Vivo* Hippocampal Ripples

Asako Noguchi,[1] **Nobuyoshi Matsumoto,**[1,2] **and Yuji Ikegaya**[1,2,3]

[1]Graduate School of Pharmaceutical Sciences, University of Tokyo, Tokyo, 113-0033, Japan, [2]Institute for AI and Beyond, University of Tokyo, Tokyo, 113-0033, Japan, and [3]Center for Information and Neural Networks, National Institute of Information and Communications Technology, Suita City, Osaka, 565-0871, Japan

Sharp-wave ripples (SWRs) are transient high-frequency oscillations of local field potentials (LFPs) in the hippocampus and play a critical role in memory consolidation. During SWRs, CA1 pyramidal cells exhibit rapid spike sequences that often replay the sequential activity that occurred during behavior. This temporally organized firing activity gradually emerges during 2 weeks after the eye opening; however, it remains unclear how the organized spikes during SWRs mature at the intracellular membrane potential (*V*m) level. Here, we recorded *V*m of CA1 pyramidal cells simultaneously with hippocampal LFPs from anesthetized immature mice of either sex after the developmental emergence of SWRs. On postnatal days 16 and 17, *V*m dynamics around SWRs were premature, characterized by prolonged depolarizations without either pre- or post-SWR hyperpolarizations. The biphasic hyperpolarizations, features typical of adult SWR-relevant *V*m, formed by approximately postnatal day 30. This *V*m maturation was associated with an increase in SWR-associated inhibitory inputs to pyramidal cells. Thus, the development of SWR-relevant inhibition restricts the temporal windows for spikes of pyramidal cells and allows CA1 pyramidal cells to organize their spike sequences during SWRs.

Key words: **development; hippocampus; *in vivo* membrane potentials; inhibition; postnatal mice; sharp-wave ripple**

Significance Statement

Sharp-wave ripples (SWRs) are prominent hippocampal oscillations and play a critical role in memory consolidation. During SWRs, hippocampal neurons synchronously emit spikes with organized temporal patterns. This temporal structure of spikes during SWRs develops during the third and fourth postnatal weeks, but the underlying mechanisms are not well understood. Here, we recorded *in vivo* membrane potentials from hippocampal neurons in premature mice and suggest that the maturation of SWR-associated inhibition enables hippocampal neurons to produce precisely controlled spike times during SWRs.

Introduction

The hippocampus is a critical brain region for representing the outer world, internalizing behavioral trajectories of animals into their mental maps (O'Keefe and Nadel, 1979; Ekstrom and Ranganath, 2018), and consolidating the acquired internal information into memory episodes (Girardeau and Zugaro, 2011). During quiet wakefulness and slow wave sleep, the hippocampus generates sharp-wave ripples (SWRs), brief (40-100 ms) and high-frequency (100-250 Hz) oscillations in local field potentials (LFPs) (Buzsáki, 2015). SWRs are associated with spikes emitted sequentially by multiple CA1 pyramidal cells, which often reflect offline reactivation of spike sequences that occurred during behavior and are believed to contribute to memory consolidation (Lee and Wilson, 2002; Girardeau and Zugaro, 2011; Foster, 2017). A recent study demonstrated that these temporally organized spikes emerged gradually during the third and fourth postnatal weeks; sequential spike patterns appear in the third postnatal week and mature enough to represent behavioral trajectories during the fourth postnatal week (Farooq and Dragoi, 2019). However, it is still unclear how the maturation of the temporally coordinated spikes during SWRs is implemented at the single-cell level.

In adult rodents, SWR-associated spikes of CA1 pyramidal cells are regulated at the subthreshold level. Pyramidal cells exhibit triphasic dynamics in the membrane potentials (*V*m), that is, pre-SWR hyperpolarization, depolarization during SWRs, and post-SWR hyperpolarization (English et al., 2014; Hulse et al., 2016; Noguchi et al., 2022). The characteristic *V*m dynamics

Received Jan. 21, 2023; revised June 23, 2023; accepted June 27, 2023.

Author contributions: A.N. and Y.I. designed research; A.N. and N.M. performed research; A.N. analyzed data; A.N. wrote the first draft of the paper; A.N., N.M., and Y.I. edited the paper; A.N. and Y.I. wrote the paper.

This work was supported by Japan Science and Technology Agency ERATO JPMJER1801; University of Tokyo Institute for AI and Beyond; and Japan Society for the Promotion of Science Grants-in-Aid for Scientific Research 18H05525 and 20K15926. The data and codes that support the findings of this study are available from the corresponding author upon reasonable request.

The authors declare no competing financial interests.

Correspondence should be addressed to Asako Noguchi at asakonoguchi.an@gmail.com.

https://doi.org/10.1523/JNEUROSCI.0125-23.2023

coordinate the characteristic inhibitory and excitatory balance around SWRs and regulate the spike times of individual neurons during SWRs. Extracellular recordings from freely behaving animals have revealed that inhibitory interneurons regulate the spike times of pyramidal cells (Stark et al., 2014, 2015; Noguchi et al., 2022). Given that CA1 interneurons are still maturing during the third and fourth postnatal weeks (Cohen et al., 2000; Doischer et al., 2008; Le Magueresse and Monyer, 2013), the maturation of local inhibitory circuits in the CA1 subregion could work as a potential driver behind the postnatal refinement of SWR-related activity. Based on this idea, we hypothesized that premature CA1 pyramidal cells exhibit different SWR-associated *V*m dynamics than mature cells.

In the present study, we recorded intracellular *V*m dynamics in CA1 pyramidal neurons from mice aged between postnatal day 16 (P16) and P40, suggesting that inhibitory synaptic inputs increase gradually during development and shape the characteristic peri-SWR *V*m dynamics, which possibly underlies the maturation of temporal organization of SWR-associated spikes in pyramidal cells during the third and fourth postnatal weeks.

Materials and Methods

Animal ethics. Animal experiments were performed with the approval of the animal experiment ethics committee at the University of Tokyo (approval number P4-4) and in accordance with the University of Tokyo guidelines for the care and use of laboratory animals. These experimental protocols were conducted in accordance with the Fundamental Guidelines for the Proper Conduct of Animal Experiments and Related Activities in Academic Research Institutions (Ministry of Education, Culture, Sports, Science and Technology, Notice No. 71 of 2006), the Standards for Breeding and Housing of and Pain Alleviation for Experimental Animals (Ministry of the Environment, Notice No. 88 of 2006), and the Guidelines on the Method of Animal Disposal (Prime Minister's Office, Notice No. 40 of 1995).

Patch-clamp and LFP recordings. Whole-cell recordings were obtained from postnatal 16- to 17- (13 male, 4 female), 21- to 22- (7 male), 27- to 28- (5 male), and 29- to 40-day-old (20 male) ICR mice (Japan) (Ishikawa et al., 2014; Funayama et al., 2015). After exposure to an enriched environment (EE) for 30 min, the mice were intraperitoneally anesthetized with 1.5 g/kg (P16-P17 and P21-P22) or 2.25 g/kg (P27-P28 and P29-P40) urethane. P16-P17 mice were not exposed to EE because they were not able to explore the environment. The control condition in Figure 5 (i.e., without exposure to EE) consisted of 9 P29-P40 male mice. Anesthesia was confirmed by the absence of paw withdrawal, whisker movement, and eyeblink reflexes. The skin was subsequently removed from the head, and a metal head-holding plate was fixed to the skull. A craniotomy was performed, the coordinates of which were altered corresponding to the size of the brain at different developmental periods. Based on the length between the bregma and the lambda (hereafter, BL length), the skull was cut into squares, with one side 5/8 × the BL length. The anteromedial corner of the square was 1/8 of the BL length placed posterior and lateral to the bregma. The neocortex above the hippocampus was subsequently aspirated (Kuga et al., 2011; Sakaguchi et al., 2012; Matsumoto et al., 2016). The exposed hippocampal window was covered with 2.0% agar at a thickness of 1.5 mm. To obtain recordings from awake mice, mice were implanted with metal head-holding plates under short-term anesthesia with 2%-3% isoflurane. After >24 h of recovery, the mice received head-fixation training on a custom-made stereotaxic fixture for 1-2 h per day. The training continued for up to 5 d until the mice learned to remain calm. LFPs were recorded from the dorsal CA1 region using a tungsten electrode (3.5-4.5 MΩ, catalog #UEWMGCSEKNNM, FHC) coated with a crystalline powder of 1,1′-dioctadecyl-3,3,3′,3′-tetramethylindocarbocyanine perchlorate DiI. Whole-cell patch-clamp recordings were obtained from neurons in the CA1 pyramidal cell layer (0.8-1.2 mm below the hippocampal window) using borosilicate glass electrodes (3-8 MΩ). Pyramidal cells were identified based on regular spiking properties in response to step-pulse current injection and morphologic features, including apical, oblique, and basal dendrites with spines, in *post hoc* histology. A cell was discarded unless it was identified as a pyramidal cell. For current-clamp recordings, the intrapipette solution consisted of the following reagents: 120 mM K-gluconate, 10 mM KCl, 10 mM HEPES, 10 mM creatine phosphate, 4 mM MgATP, 0.3 mM Na2GTP, 0.2 mM EGTA, pH 7.3, and 0.2% biocytin. Cells were discarded when the mean resting potential exceeded −55 mV and the action potentials were <−20 mV. For voltage-clamp recordings, the intrapipette solution consisted of the following reagents: 130 mM CsMeSO4, 10 mM CsCl, 10 mM HEPES, 10 mM phosphocreatine, 4 mM MgATP, 0.3 mM NaGTP, 10 mM QX-314, and 0.2% biocytin. Cells were discarded if the access resistance exceeded 60 MΩ. Signals recorded by LFP electrodes were amplified using a DAM80 AC differential amplifier (World Precision Instruments). Signals recorded by patch-clamp electrodes were amplified using MultiClamp 700B amplifiers. Both types of signals were digitized at a sampling rate of 20 kHz using a Digidata 1440A digitizer that was controlled by pCLAMP 10.3 software (Molecular Devices).

Histology. Following each experiment, the electrode was carefully withdrawn from the hippocampus. The mice were transcardially perfused with 4% PFA followed by overnight postfixation. The brains were coronally or sagittally sectioned at a thickness of 100 μm using a vibratome. The sections were incubated with 2 μg/ml streptavidin-AlexaFluor-594 conjugate and 0.2% Triton X-100 for 4 h, followed by incubation with 0.4% NeuroTrace 435/455 blue fluorescent Nissl stain (N21479; Fisher Scientific) for 2-4 h. The locations of LFP electrodes were also detectable via DiI fluorescence. Fluorescence images were acquired using an FV1200 (Olympus) or A1 HD25 (Nikon) confocal microscope and were subsequently merged.

Data analysis. Data were analyzed offline using custom-made MATLAB (R2017b, The MathWorks) routines. The summarized data are reported as the mean ± SEM unless otherwise specified. For box plots, the centerline shows the median, the box boundaries indicate the upper and lower quartiles, and the whiskers cover the 10th-90th percentiles. For correlation plots, the significance was determined based on Pearson's correlation coefficient and a *t* test of the correlation coefficients. $p < 0.05$ was considered statistically significant. All statistical tests were two-sided.

SWR analysis. To detect SWRs from LFP traces recorded by a tungsten electrode, LFP traces were downsampled to 500 Hz and bandpass filtered between 100 and 250 Hz. Ripples, referred to here as SWRs, were detected at a threshold of 3 × SD of the baseline noise (Mizunuma et al., 2014). The detected events were subsequently scrutinized by eye and manually rejected if the detection was erroneous. The ripple power and frequency for each SWR event were calculated as the maximum power and its frequency between 100 and 250 Hz after the fast Fourier transform analyses of the raw traces.

ΔVm analysis. Spikes were detected as peaks during periods with *V*m values >−20 mV in raw 20 kHz traces of whole-cell recordings. To average subthreshold *V*m values, spikes were truncated as follows: (1) raw *V*m traces were smoothed using a moving average with a window of 1 ms; (2) the minimum index at which the rate of change exceeded 4 V/s was detected as the leading edge of a spike; and (3) traces were linearly interpolated from the leading edge until the time point that first showed a *V*m value below the edge value. When multiple edges, such as those of complex spikes, were detected within a period of 30 ms, these edges were individually interpolated from the previous edge until the next time point that first showed a *V*m value below the edge value. They were aligned to the SWR onset times and additively averaged across SWRs.

To quantify FWHM values of depolarizations during SWRs, we detected the highest peak value of *V*m between −20 and 120 ms relative to the SWR onset time as the maximum. As the baseline *V*m, *V*m values between −2000 and −1000 ms relative to the SWR onset time were averaged. For the SWR events in which the maximum was above the baseline *V*m values, FWHM values were calculated. To quantify ΔVm_{pre} and ΔVm_{post}, we identified the time point that gave the minimum *V*m value between −50 and 0 ms or 100 and 200 ms relative to the SWR onset time (pre-SWR or post-SWR periods, respectively). *V*m values were averaged

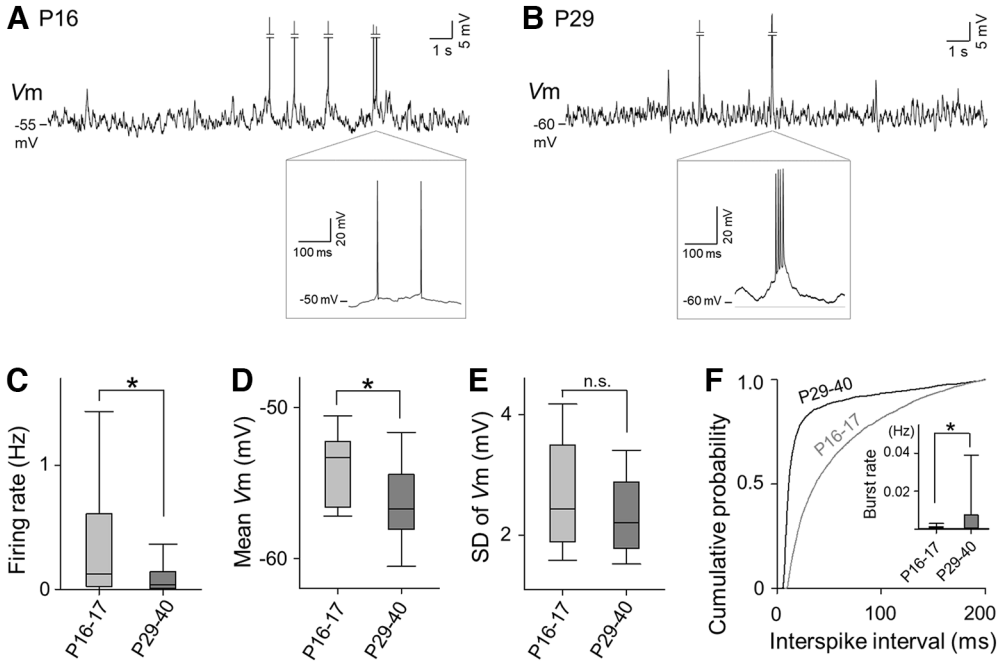

Figure 1. Comparison of spiking and *V*m dynamics of *in vivo* hippocampal CA1 pyramidal cells between P16-P17 and P29-P40 mice. ***A***, A representative *V*m trace of a hippocampal CA1 pyramidal neuron recorded from a P16 mouse, a part of which is enlarged in the bottom box. ***B***, Same as in ***A***, but from a P29 mouse. ***C***, Firing rates were higher on P16-P17 than on P29-P40. $p = 0.013$, $t_{(64)} = 2.6$, Student's *t* test. $n = 22$ and 44 cells for P16-P17 and P29-P40, respectively. ***D***, Mean *V*m values were higher on P16-P17 than on P29-P40. $p = 0.0041$, $t_{(64)} = 3.0$, Student's *t* test. $n = 22$ and 44 cells for P16-P17 and P29-P40, respectively. ***E***, The SDs of *V*m did not differ between P16-P17 and P29-P40. $p = 0.12$, $t_{(64)} = 1.6$, Student's *t* test. $n = 22$ and 44 cells for P16-P17 and P29-P40, respectively. ***F***, Cumulative probability distributions of ISIs differed between P16-P17 and P29-P40. Data are displayed in the range of $\leq$200 ms. $p = 3.1 \times 10^{-246}$, $D = 0.51$, two-sample Kolmogorov–Smirnov test. $n = 3807$ and 1539 intervals for P16-P17 and P29-P40, respectively. Inset, The event rates of burst spikes (ISI $<$ 8 ms) were lower on P16-P17 than on P29-P40. $p = 0.026$, $t_{(64)} = -2.3$, Student's *t* test. $n = 22$ and 44 cells for P16-P17 and P29-P40, respectively.

between −25 and 25 ms relative to these time points, and the baseline *V*m value was subtracted to obtain ΔVm_{pre} and ΔVm_{post}, respectively. ΔVm_{during} was obtained by subtracting the baseline *V*m value from the maximum *V*m value between 0 and 100 ms relative to the SWR onset time (during-SWR period).

For SWR-triggered analysis of excitatory and inhibitory postsynaptic conductances (EPSGs and IPSGs, respectively), we took a postsynaptic current at a given time between −2000 and 400 ms relative to the SWR onset and subtracted the mean current between −2000 and −1000 ms. The current traces were averaged across SWRs. EPSGs and IPSGs were calculated as $I_{E/I}/(V_h - E_{rev,\ E/I})$, where $I_{E/I}$ is the excitatory/inhibitory current at a given time; V_h is the holding potential of −70 and 10 mV for EPSGs and IPSGs, respectively (Gan et al., 2017); and $E_{rev,\ E/I}$ are the reversal potentials of 0 and −90 mV for EPSGs and IPSGs, respectively (Funayama et al., 2016).

Results

Higher membrane excitability and fewer spike bursts in premature hippocampal neurons

To examine developmental changes in SWR-associated *V*m dynamics of hippocampal neurons, we conducted *in vivo* whole-cell patch-clamp recordings from dorsal hippocampal CA1 pyramidal cells simultaneously with LFP recordings in the CA1 region of immature mice. Recordings were excluded from subsequent analyses if *post hoc* biocytin-based visualization, their recording sites, or their firing properties failed to identify the recorded neurons as CA1 pyramidal cells (Noguchi et al., 2022). SWRs start to emerge after the end of the second postnatal week (Buhl and Buzsáki, 2005). Indeed, we did not detect SWRs in mice younger than P15 ($n = 6$ mice) based on the same detection criteria used in adult mice. Thus, we collected data from mice older than P15. As a result, we recorded *V*ms from 22, 14, 9, and 44 patch-clamped cells in a total of 17 (13 male, 4 female), 7, 5, and 20 male mice, respectively, aged P16-P17, P21-P22, P27-P28, and P29-P40. Recording periods ranged from 162 to 2749 s (median = 586 s), 147 to 2116 s (median = 890 s), 420 to 1380 s (median = 496 s), and 113 to 2097 s (median = 546 s), during which a total of 240, 664, 385, and 1882 SWRs, respectively, were detected in LFPs.

We first compared the subthreshold *V*m recorded from immature (P16-P17) and adult (P29-P40) mice, regardless of SWR occurrence (Fig. 1*A*,*B*). P16-P17 mice showed significantly higher firing rates (0.42 ± 0.13 Hz) than P29-P40 mice (0.14 ± 0.045 Hz), indicating higher excitability of immature pyramidal cells (Fig. 1*C*, $p = 0.013$, $t_{(64)} = 2.6$, Student's *t* test, $n = 22$ and 44 cells for P16-P17 and P29-P40, respectively). Consistently, the mean *V*m values were significantly higher in P16-P17 mice (−54 ± 0.57 mV) than in P29-P40 mice (−57 ± 0.53 mV) (Fig. 1*D*, $p = 0.0041$, $t_{(64)} = 3.0$, Student's *t* test, $n = 22$ and 44 cells for P16-P17 and P29-P40, respectively). The fluctuations in *V*m, captured by the SDs, did not differ between immature (2.7 ± 0.21 mV) and adult mice (2.3 ± 0.11 mV) (Fig. 1*E*, $p = 0.12$, $t_{(64)} = 1.6$, Student's *t* test, $n = 22$ and 44 cells for P16-P17 and P29-P40, respectively). Notably, burst-like firing activity was observed in both developmental periods (Fig. 1, insets), but the interspike intervals (ISIs) of the burst-like activity were larger on P16-P17 (56 ± 0.77 ms) than on P29-P40 (25 ± 0.96 ms) (Fig. 1*F*, $p = 3.1 \times 10^{-246}$, $D = 0.51$, two-sample Kolmogorov–Smirnov test for the cumulative distributions of ISIs $<$200 ms, $n = 3807$ and 1539 intervals on P16-P17 and P29-P40, respectively). Larger ISIs on P16-P17 suggest fewer bursty spikes in immature mice. We defined a series of successive spikes with ISIs $<$8 ms as a burst event and calculated the frequency of burst events for each cell (Harris et al., 2001; Mizuseki and

Buzsáki, 2013). The burst event rates were significantly lower on P16-P17 ($8.8 \times 10^{-4} \pm 3.5 \times 10^{-4}$ Hz) than on P29-P40 (0.0093 ± 0.0026 Hz) (Fig. 1*F*, inset, $p = 0.026$, $t_{(64)} = -2.3$, Student's *t* test, $n = 22$ and 44 cells for P16-P17 and P29-P40, respectively). These results indicate that, at the beginning of SWR emergence, hippocampal CA1 pyramidal neurons exhibit high excitability with higher spontaneous spike rates but rarely fire spikes at frequencies higher than ~100 Hz.

Maturation of SWRs throughout the third and fourth postnatal weeks

We investigated the maturation of SWR events during development. As shown in the representative LFP traces in Figure 2*A*, *B*, the SWR event frequency was higher in older mice. As summarized in Figure 2*C*, the data showed a significant increase during the fourth postnatal week (Fig. 2*C*, $p < 0.05$, one-way ANOVA followed by Tukey–Kramer *post hoc* test, 0.013 ± 0.0022, 0.043 ± 0.011, 0.091 ± 0.024, and 0.16 ± 0.019 Hz, $n = 22$, 14, 5, and 20 datasets for P16-P17, P21-P22, P27-P28, and P29-P40, respectively). Similar results were obtained for the ripple power (5.2 ± 0.34, 3.3 ± 0.13, 17 ± 1.0, and 16 ± 0.53 μV^2 for P16-P17, P21-P22, P27-P28, and P29-P40, respectively) and frequency (114 ± 0.96, 114 ± 0.73, 118 ± 0.80, and 117 ± 0.37 Hz for P16-P17, P21-P22, P27-P28, and P29-P40, respectively) but not for the SWR duration (70 ± 2.1, 65 ± 0.86, 72 ± 1.6, and 71 ± 2.8 ms for P16-P17, P21-P22, P27-P28, and P29-P40, respectively) (Fig. 2*D–F*, $p < 0.05$, one-way ANOVA followed by Tukey–Kramer *post hoc* test, $n = 246$, 593, 386, and 1881 SWRs for P16-P17, P21-P22, P27-P28, and P29-P40, respectively).

In addition to the change in the characteristics of individual SWRs, we noticed that successive SWRs (Davidson et al., 2009; Yamamoto and Tonegawa, 2017; Oliva et al., 2018) occurred more frequently in adult mice than in P16-P17 mice (Fig. 2*A*,*B*). To quantitatively define successive SWRs, we determined the upper threshold of interevent intervals (IEIs) based on the pooled distribution of IEIs for all recorded SWR events (Fig. 2*G*). Specifically, the distribution of IEIs less than the mode was fitted with a half-Gaussian distribution and folded around the mode value (Fig. 2*G*, black), which was designated as a population of successive SWRs. The remaining distribution after subtracting this distribution from the entire distribution was considered sporadic SWRs (Fig. 2*G*, white). The receiver-operating characteristic curve was drawn based on the ratios of the two distributions to the entire distribution of IEIs <1 s, and the threshold IEI for detecting successive SWRs was set to 250 ms, as this enabled the best separation of the two distributions (Fig. 2*G*, inset). The ratios of successive SWRs to total SWRs were higher in older mice (Fig. 2*H*, 54/246, 187/593, 240/386, and 945/1881 SWRs for P16-P17, P21-P22, P27-P28, and P29-P40, respectively, $p = 8.9 \times 10^{-31}$, $\chi^2 = 1.4 \times 10^2$, χ^2 test). Thus, SWRs gradually matured throughout the third and fourth postnatal weeks.

Weak SWR selectivity of spikes in immature hippocampal neurons

We compared SWR-associated firing activity of CA1 pyramidal neurons between the ages of P16-P17 and P29-P40 (Fig. 3*A*). In contrast to the overall firing rates (Fig. 1*C*), the mean firing rates in pre-SWR periods (0-50 ms before SWR onset; 0.061 ± 0.038 and 0.37 ± 0.096 Hz for P16-P17 and P29-P40, respectively) and during-SWR periods (0-100 ms after SWR onset; 1.7 ± 0.98 and 6.2 ± 0.93 Hz for P16-P17 and P29-P40, respectively) were significantly lower on P16-P17 than on P29-P40, while

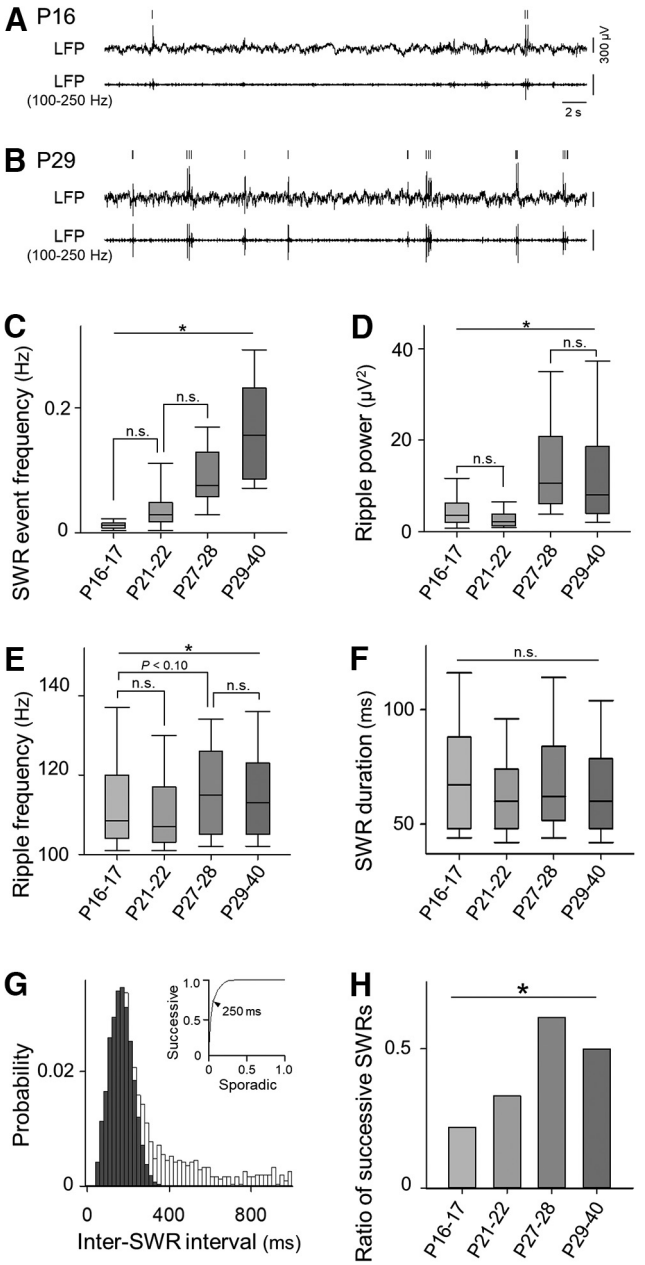

Figure 2. Developmental changes in SWR characteristics. ***A***, A representative raw trace of hippocampal LFPs recorded from a P16 mouse (top), bandpass-filtered between 100 and 250 Hz (bottom). Ticks above the traces indicate the onset times of SWRs. ***B***, Same as in ***A***, but from a P29 mouse. ***C***, The SWR event frequency increased with increased postnatal days. *$p < 0.05$ (Tukey–Kramer *post hoc* test following one-way ANOVA). $n = 22$, 14, 5, and 20 datasets for P16-P17, P21-P22, P27-P28, and P29-P40, respectively. ***D–F***, Same as in ***C***, but for the power (***D***) and frequency (***E***) of ripples and the duration of SWRs (***F***). $n = 246$, 593, 386, and 1881 SWRs for P16-P17, P21-P22, P27-P28, and P29-P40, respectively. ***G***, Probability distribution of inter-SWR intervals. The distribution of values smaller than the distribution peak (mode) was fitted with a half-Gaussian distribution and folded against the mode (black). White distribution represents the remaining distribution after subtracting the estimated Gaussian (black) distribution. Then, the distribution of inter-SWR intervals was divided into two distributions: successive SWRs (black) and sporadic SWRs (white). Inset, Receiver-operating characteristic curve with the probabilities of the intervals of successive SWRs as the vertical axis and the probabilities of the intervals of sporadic SWRs as the horizontal axis. The optimal cutoff was found to be 250 ms, which was set as the threshold of SWR bursts in this study. ***H***, Developmental changes in the ratios of successive SWRs to the total SWRs. $p = 6.8 \times 10^{-13}$, $\chi^2 = 59.7$, χ^2 test, 22, 14, 5, and 20 datasets for P16-P17, P21-P22, P27-P28, and P29-P40, respectively.

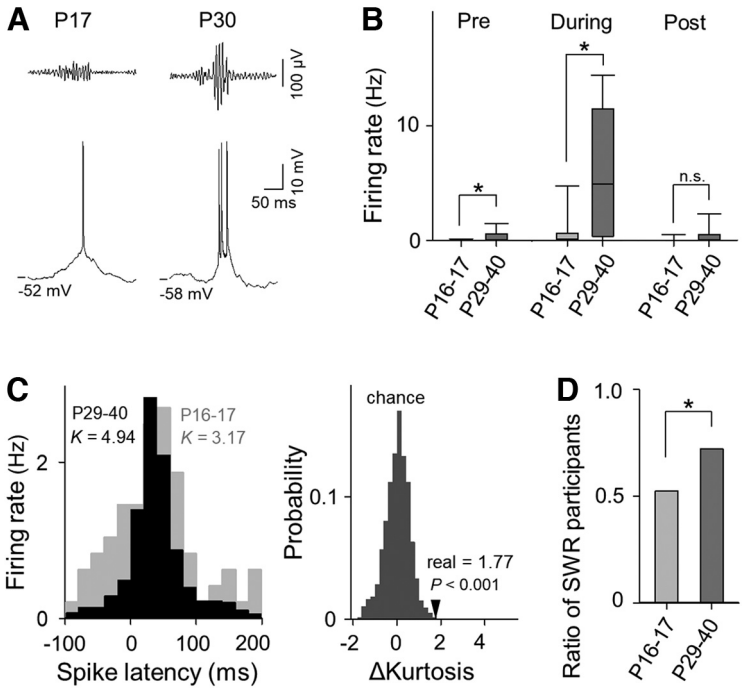

Figure 3. Comparison of firing activity between P16-P17 and P29-P40 mice. ***A***, Representative traces of 100-250-Hz bandpass-filtered LFPs (top) and *Vm* (bottom) during a SWR recorded from P17 and P30 mice. ***B***, Pre-, during-, and post-SWR firing rates were all higher on P16-P17 than on P29-P40. $p = 0.028$, 0.0037, and 0.21, $t_{(64)} = -2.3$, -3.0, and -1.3, Student's *t* test, for pre-, during, and post-SWR periods, respectively. $n = 22$ and 44 cells for P16-P17 and P29-P40, respectively. ***C***, Left, The distributions of spike latencies relative to the SWR onsets on P16-P17 (gray) showed smaller kurtosis ($K = 3.17$) than those on P29-P40 (black, $K = 4.94$). Right, The difference in the kurtosis (ΔKurtosis = 1.77) of the distributions of spike latencies between P16-P17 and P29-P40 (real), calculated from the left panel, was significantly larger than the chance level that was obtained from 1000 surrogates produced by randomly dividing the pooled spike latencies into two groups with the same numbers as the real data. ***D***, The ratio of cells that participated significantly in SWRs to the total recorded cells was significantly higher on P29-P40 than on P16-P17. $p = 0.042$, $\chi^2 = 4.1$, χ^2 test. $n = 22$ and 44 cells for P16-P17 and P29-P40, respectively.

the mean firing rates in post-SWR periods (100-200 ms after SWR onset; 0.23 ± 0.16 and 0.64 ± 0.21 Hz for P16-P17 and P29-P40, respectively) did not differ according to age (Fig. 3*B*, $p = 0.028$, 0.0037 and 0.21, $t_{(64)} = -2.3$, -3.0, and -1.3 for pre-, during, and post-SWR periods, Student's *t* test, $n = 22$ and 44 cells for P16-P17 and P29-P40, respectively). Thus, mature pyramidal cells were likely to fire spikes more selectively during SWRs. Consistent with this idea, the distribution of spike latencies relative to SWR onsets exhibited a sharper peak, and its kurtosis was larger on P29-P40 than on P16-P17 (Fig. 3*C*, left). To statistically assess the difference in the two kurtosis values (ΔKurtosis), all spike latencies were pooled from P16-P17 and P29-P40 mice and were randomly reassigned to two groups with the same number of values as the real data. Then, ΔKurtosis was calculated for the resampled groups. This procedure was repeated 1000 times to generate a null distribution. The real ΔKurtosis value was larger than the maximum of the null distribution (Fig. 3*C*, right, $p < 10^{-3}$), indicating that spikes were more time-locked to SWRs on P29-P40 than on P16-P17.

We next quantified the number of pyramidal cells with significant increases in firing rates during SWRs. For each cell, the number of during-SWR spikes was compared with its null distribution, which was calculated from 1000 randomized surrogates in which spike times were randomly shifted within the recording period. Cells that had numbers of during-SWR spikes that exceeded the upper bound of the 95% CIs of the null distributions were regarded as SWR participants. Of all recorded cells on P16-P17 and P29-P40, 11/22 cells and 26/44 cells were SWR participants, the ratio of which was significantly higher on P29-P40 (Fig. 3*D*, $p = 0.042$, $\chi^2 = 4.1$, χ^2 test). Therefore, immature CA1 pyramidal cells exhibit more spontaneous activity, but the temporal selectivity of their spikes to SWRs is lower than mature pyramidal neurons.

Developmental increases in SWR-associated hyperpolarization

To explore mechanisms underlying the lack of temporal specificity of SWR-associated spikes in immature neurons, we focused on subthreshold *Vm* dynamics (Valero et al., 2015; Hulse et al., 2016; Noguchi et al., 2022). First, all *Vm* traces around SWR events were aligned to SWR onsets and averaged for cells during the four developmental periods (i.e., P16-P17, P21-P22, P27-P28, and P29-P40; Fig. 4*A*). Consistent with previous reports (Hulse et al., 2016; Noguchi et al., 2022), the averaged trace in adult mice consisted of four components: (1) slow depolarization starting ~1 s before SWR onset, (2) transient hyperpolarization ~50 ms before SWR onset, (3) large depolarization during SWRs, and (4) hyperpolarization immediately after SWRs (Fig. 4*A*, bottom). Notably, the averaged *Vm* trace of P16-P17 mice lacked prominent hyperpolarization both before and after SWRs, and the SWR-related depolarization had a longer duration than that in adult mice (Fig. 4*A*, top). The FWHM of depolarizations was smaller in older mice (Fig. 4*B*, $p < 0.05$, one-way ANOVA followed by Tukey–Kramer *post hoc* test, 63 ± 4.6, 62 ± 2.5, 45 ± 0.82, and 43 ± 0.47 ms, $n = 215$, 516, 778, and 3782 SWRs for P16-P17, P21-P22, P27-P28, and P29-P40, respectively). The longer depolarizations of immature neurons may contribute to the lower selectivity of SWR-related spikes.

We next quantified the *Vm* changes (Δ*Vm*) for pre-, during, and post-SWR periods (ΔVm_{pre}, ΔVm_{during}, and ΔVm_{post}, respectively). In the three parameters, ΔVm_{pre} (0.89 ± 0.17, 0.37 ± 0.10, 0.037 ± 0.068, and -0.20 ± 0.028 mV for P16-P17, P21-P22, P27-P28, and P29-P40, respectively) and ΔVm_{post} (-0.27 ± 0.19,

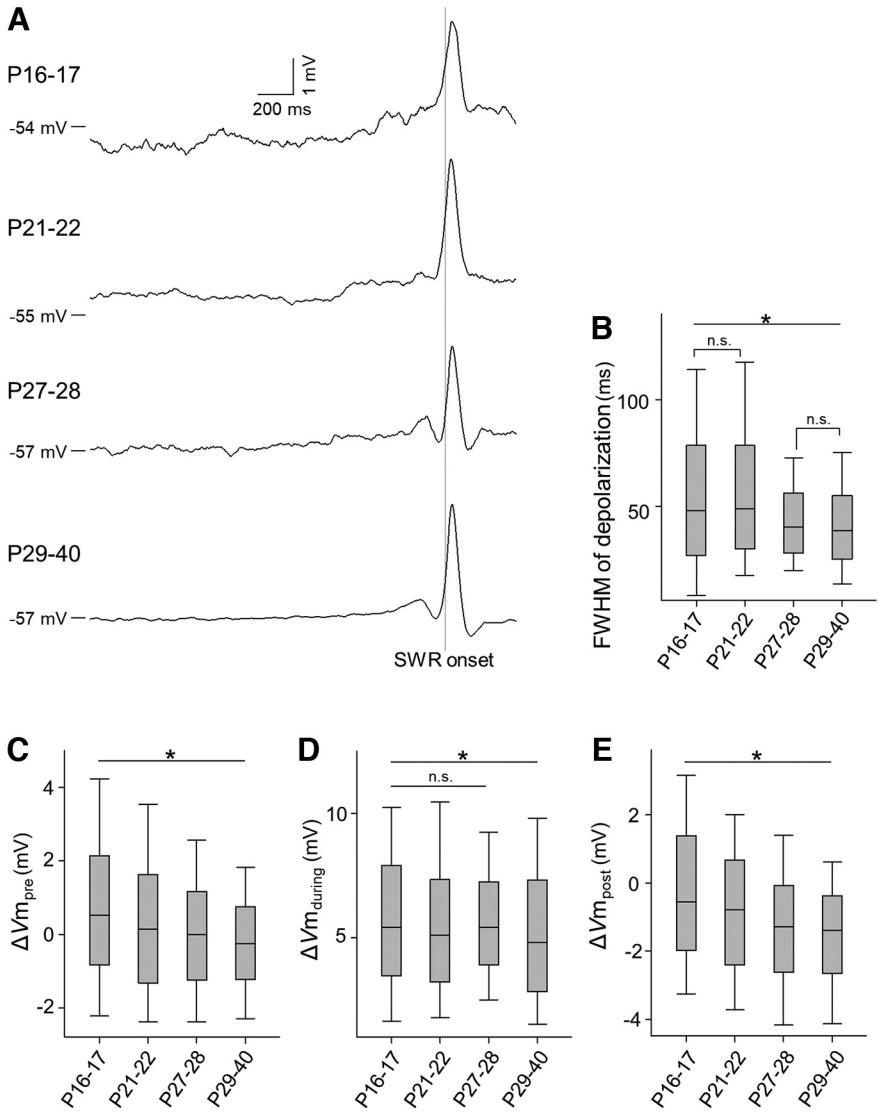

Figure 4. Developmental changes in peri-SWR *V*m dynamics. ***A***, For P16-P17, P21-P22, P27-P28, and P29-P40, a total of 239, 593, 801, and 4138 *V*m traces, respectively, in 22, 14, 9, and 44 cells from 15, 7, 5, and 20 mice were averaged relative to the SWR onsets (gray vertical lines). ***B***, FWHM values of depolarizations decreased during the fourth postnatal week. $*p < 0.05$ (Tukey–Kramer *post hoc* test after one-way ANOVA). $n = 215$, 516, 778, and 3782 SWRs for P16-P17, P21-P22, P27-P28, and P29-P40, respectively. ***C***, ΔVm_{pre} decreased with age throughout the developmental period. ***D***, ΔVm_{during} decreased after the fourth postnatal week. ***E***, ΔVm_{post} decreased with age throughout the developmental period. $*p < 0.05$ (Tukey–Kramer *post hoc* test after one-way ANOVA). $n = 246$, 595, 836, and 4159 SWRs in 22, 14, 9, and 44 cells from 15, 7, 5, and 20 mice for P16-P17, P21-P22, P27-P28, and P29-P40, respectively.

-0.80 ± 0.10, -1.3 ± 0.074, and -1.6 ± 0.032 mV for P16-P17, P21-P22, P27-P28, and P29-P40, respectively) gradually decreased with age, which indicates that more mature CA1 pyramidal cells received larger inhibitory inputs during pre- and post-SWR periods (Fig. 4*C–E*, $p < 0.05$, one-way ANOVA followed by Tukey–Kramer *post hoc* test, $n = 246$, 593, 836, and 4159 SWRs for P16-P17, P21-P22, P27-P28, and P29-P40, respectively). For all the parameters described above, we found no difference between neuronal activity on P16 and P17 (data not shown). These results suggest that the maturation of peri-SWR inhibition restricts the temporal window for pyramidal cells to emit spikes during SWRs, which eventually enables the generation of temporally organized activity in mature mice.

Possible confounding factors for the development of *V*m dynamics

Postnatal changes in *V*m dynamics may be influenced by experimental conditions that vary because of differences in the physical maturity of mice. These conditions include exposure to an EE and the dose of urethane anesthesia.

Before anesthesia, mice older than P21 were exposed to EE for 30 min, which increased the frequency of SWR events (Fig. 5*A*, 0.033 ± 0.018 and 0.16 ± 0.019 Hz; $n = 5$ and 20 datasets without and with EE, respectively; $p = 9.4 \times 10^{-4}$, $t_{(23)} = -3.73$, Student's *t* test). Mice on P16-P17 were not exposed to EE because they were physically incapable of exploring the environment because of immaturity. To investigate the impact of EE on neuronal activity, we compared spontaneous and SWR-related activity of pyramidal cells in adult mice with and without exposure to EE. The results showed that the mean firing rates were higher (Fig. 5*B*, 0.54 ± 0.23 and 0.14 ± 0.045 Hz; $n = 9$ and 44 cells without and with EE, respectively; $p = 0.0066$, $t_{(51)} = -2.8$, Student's *t* test), and that ISIs were larger in adult mice without EE than in those with EE (Fig. 5*E*, 42 ± 2.0 and 25 ± 0.96 ms; $n = 9$ and 44 cells without and with EE, respectively; $p = 3.8 \times 10^{-59}$, $D = 0.43$, two-sample Kolmogorov–Smirnov test), suggesting that exposure to EE may lead to

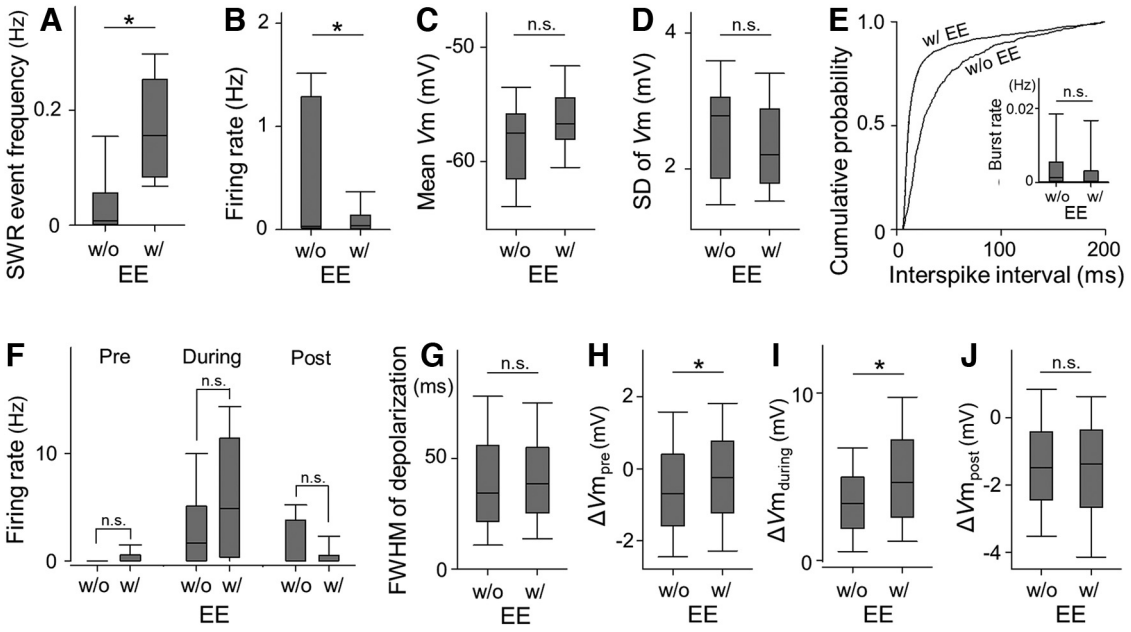

Figure 5. Effects of EEs on neuronal activity. ***A***, The SWR event frequency was higher in adult mice exposed to EEs than in those without EE. $p = 9.4 \times 10^{-4}$, $t_{(23)} = -3.7$, Student's *t* test. $n = 5$ and 20 datasets without and with EE, respectively. ***B***, Firing rates were higher in mice without EE than in those with EE. $p = 0.0066$, $t_{(51)} = -2.8$. ***C***, ***D***, The means and SDs of *Vm* values did not differ according to EE exposure. $p = 0.18$ and 0.50, $t_{(51)} = 1.4$ and -0.68 for ***B*** and ***C***, respectively. ***A–C***, Student's *t* test. $n = 9$ and 44 cells from 9 and 20 mice without and with EE, respectively. ***E***, Cumulative probability distributions of ISIs were different between mice without and with EE. Data are displayed in the range of $\leq$200 ms. $p = 3.8 \times 10^{-59}$, $D = 0.43$, two-sample Kolmogorov–Smirnov test. $n = 466$ and 1539 intervals for without and with EE conditions, respectively. Inset, The event rates of burst spikes (ISI < 8 ms) were lower in mice with EE than in those without EE. $p = 0.99$, $t_{(51)} = 0.016$, Student's *t* test. $n = 9$ and 44 cells for 9 and 20 mice without and with EE, respectively. ***F***, Pre-, during-, and post-SWR firing rates did not differ according to EE exposure. $p = 0.20$, 0.28, and 0.15, $t_{(47)} = -1.3$, -1.1, and 1.5 for pre-, during, and post-SWR periods, respectively. $n = 5$ and 44 cells for mice without and with exposure to EE, respectively. ***G***, FWHM values of depolarizations did not differ according to EE exposure. $p = 0.37$, $t_{(3892)} = 0.89$. $n = 112$ and 3782 SWRs for mice without and with EE, respectively. ***H***, ΔVm_{pre} was larger in mice with EE than in those without EE. $p = 0.045$, $t_{(4283)} = 2.0$. $n = 126$ and 4159 SWRs for mice without and with EE, respectively. ***I***, ΔVm_{during} was larger in mice with EE than in those without EE. $p = 1.9 \times 10^{-7}$, $t_{(4279)} = 5.22$. $n = 125$ and 4156 SWRs for mice without and with EE, respectively. ***J***, ΔVm_{post} did not differ according to EE exposure. $p = 0.64$, $t_{(4283)} = -0.47$. $n = 126$ and 4159 SWRs for mice without and with EE, respectively. ***F-J***, Student's *t* test. $n = 5$ and 20 mice without and with exposure to EE, respectively.

frequent firings of pyramidal cells without high temporal resolution, similar to the firing of those observed in P16-P17 mice. No significant differences were observed in the mean *V*m (Fig. 5*C*, -58 ± 1.3 and -57 ± 0.53 mV without and with EE, respectively, $p = 0.18$, $t_{(51)} = 1.4$, Student's *t* test, $n = 9$ and 44 cells without and with EE, respectively), the SD of *V*m (Fig. 5*D*, 2.5 ± 0.027 and 2.3 ± 0.11 mV without and with EE, respectively, $p = 0.50$, $t_{(51)} = -0.68$), burst rates (Fig. 5*E*, inset, 0.0092 ± 0.0050 and 0.0093 ± 0.0026 Hz without and with EE, respectively, $p = 0.99$, $t_{(51)} = 0.016$), pre-SWR firing rates (0 and 0.37 ± 0.096 Hz without and with EE, respectively), during-SWR firing rates (3.0 ± 1.2 and 6.2 ± 0.93 Hz without and with EE, respectively), and post-SWR firing rates (1.7 ± 1.1 and 0.64 ± 0.21 Hz without and with EE, respectively) (Fig. 5*F*, $p = 0.20$, 0.28, and 0.15, $t_{(47)} = -1.3$, -1.1 and 1.5 for pre-, during-, and post-SWR periods, respectively, Student's *t* test, $n = 5$ and 44 cells without and with EE, respectively), the FWHM values of depolarizations (Fig. 5*G*, 41 ± 2.6 and 43 ± 0.47 ms without and with EE, respectively, $p = 0.37$, $t_{(3892)} = 0.89$, $n = 112$ and 3782 SWRs without and with EE, respectively), and ΔVm_{post} (Fig. 5*J*, -1.5 ± 0.17 and -1.6 ± 0.032 mV without and with EE, respectively, $p = 0.64$, $t_{(4283)} = -0.47$, $n = 126$ and 4159 SWR without and with EE, respectively) between mice with and without EE, indicating that EE does not affect the intrinsic properties and SWR-related firing activity of pyramidal cells. Furthermore, mice without EE showed smaller ΔVm_{pre} (Fig. 5*H*, -0.53 ± 0.15 and -0.20 ± 0.028 mV without and with EE, respectively, $p = 0.045$, $t_{(4282)} = 2.0$, $n = 125$ and 4159 SWRs without and with EE, respectively) and ΔVm_{during} than mice with EE (Fig. 5*I*, 3.5 ± 0.23 and 5.1 ± 0.053 mV without and with EE, respectively, $p = 1.9 \times 10^{-7}$, $t_{(4279)} = 5.2$, $n = 125$ and 4156 SWRs without and with EE, respectively), indicating that EE exposure led to less mature *V*m dynamics around SWRs. Thus, transient exposure to EE was unlikely to be a confounding factor for the developmental changes observed in SWR-related *V*m dynamics. Nevertheless, it is still possible that the mature *V*m dynamics reported in this study resulted from the physical maturation of the animals, which enabled them to explore the environment. This possibility should be investigated in future experiments.

We administered intraperitoneal doses of 1.5 and 2.25 g/kg urethane to mice aged P16-P22 and P27-P40, respectively, as the minimum required doses. To investigate whether the doses of anesthesia differentially affected the neuronal dynamics according to age, we compared the activity of pyramidal cells in awake and urethane-anesthetized adult mice. Firing rates were higher in awake mice than in anesthetized mice (Fig. 6*A*, 0.42 ± 0.22 and 0.14 ± 0.045 Hz for awake and anesthetized mice, respectively, $p = 0.044$, $t_{(51)} = 2.1$, Student's *t* test, $n = 9$ and 44 cells for awake and anesthetized mice, respectively), while the mean *V*m did not differ between the two conditions (Fig. 6*B*, -56 ± 1.2 and -57 ± 0.53 mV for awake and anesthetized mice, respectively, $p = 0.78$, $t_{(51)} = 0.27$). The SD of *V*m was larger in awake mice (Fig. 6*C*, 3.0 ± 0.40 and 2.3 ± 0.11 mV for awake and anesthetized mice, respectively, $p = 0.028$, $t_{(51)} = 2.3$). Notably, the ISI was smaller (Fig. 6*D*, 17 ± 1.3 and 25 ± 0.96 ms for awake and anesthetized mice, respectively, $p = 3.8 \times 10^{-57}$, $D = 0.40$, two-sample Kolmogorov–Smirnov test, $n = 560$ and 1539 ISIs from 9 awake and 20 anesthetized mice, respectively), and

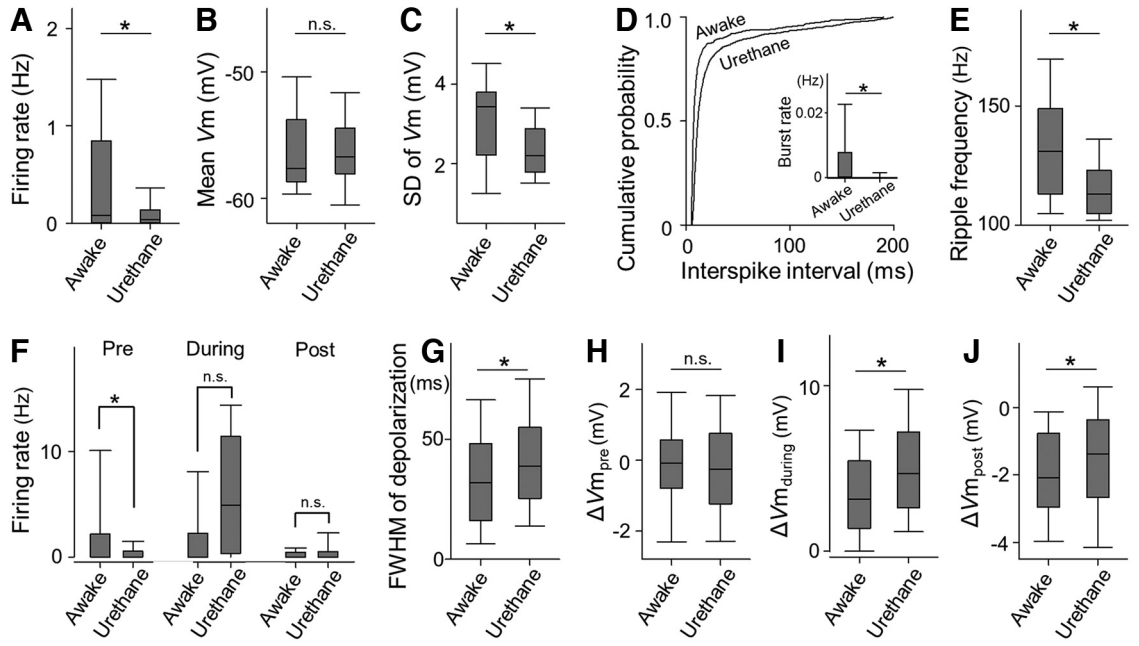

Figure 6. Effect of urethane anesthesia on neuronal activity. ***A***, Firing rates were higher in awake mice than in urethane-anesthetized mice. $p = 0.044$, $t_{(51)} = 2.1$. ***B***, Mean *V*m values did not differ between awake and anesthetized mice. $p = 0.78$, $t_{(51)} = 0.27$. ***C***, The SDs of *V*m values were larger in awake mice than in anesthetized mice. $p = 0.028$, $t_{(51)} = 2.3$. ***A–C***, Student's *t* test. $n = 9$ and 44 cells from 9 awake and 20 anesthetized mice, respectively. ***D***, Cumulative probability distributions of ISIs were different between awake and anesthetized mice. Data are displayed in the range of ≤200 ms. $p = 3.8 \times 10^{-57}$, $D = 0.40$, two-sample Kolmogorov–Smirnov test. $n = 560$ and 1539 intervals from 9 awake and 20 anesthetized mice, respectively. Inset, The event rates of burst spikes (ISI < 8 ms) were lower in anesthetized mice than in awake mice. $p = 7.4 \times 10^{-4}$, $t_{(51)} = -3.6$, Student's *t* test. $n = 9$ and 44 cells from 9 awake and 20 anesthetized mice, respectively. ***E***, Ripple frequency was higher in awake mice than in anesthetized mice. $p = 1.4 \times 10^{-49}$, $t_{(2121)} = 15.0$, Student's *t* test. $n = 241$ and 1882 SWRs from 9 awake and 20 anesthetized mice, respectively. ***F***, Pre-SWR firing rates were higher in awake mice than in anesthetized mice. During- and post-SWR firing rates did not differ between the two conditions. $p = 0.010$, 0.054, 0.39, $t_{(51)} = 2.7$, −2.0, and −0.87 for pre-, during, and post-SWR periods, respectively. Student's *t* test. $n = 9$ and 44 cells from awake and anesthetized mice, respectively. ***G***, FWHM values of depolarizations were larger in anesthetized mice than in awake mice. $p = 2.1 \times 10^{-5}$, $t_{(3984)} = -4.3$. $n = 204$ and 3782 SWRs from awake and anesthetized mice, respectively. ***H***, ΔVm_{pre} did not differ between awake and anesthetized mice. $p = 0.30$, $t_{(4398)} = 1.0$. $n = 241$ and 4159 SWRs from awake and anesthetized mice, respectively. ***I***, ΔVm_{during} was larger in anesthetized mice than in awake mice. $p = 1.4 \times 10^{-10}$, $t_{(4386)} = -6.4$. $n = 241$ and 4147 SWRs from awake and anesthetized mice, respectively. ***J***, ΔVm_{post} was larger in anesthetized mice than in awake mice. $p = 4.8 \times 10^{-4}$, $t_{(4398)} = -3.5$. $n = 241$ and 4159 SWRs from awake and anesthetized mice, respectively. ***E–I***, Student's *t* test. $n = 9$ awake and 20 anesthetized mice, respectively.

burst rates were higher in awake mice than in anesthetized mice (Fig. 6*D*, inset, 0.11 ± 0.063 and 0.0093 ± 0.0026 Hz for awake and anesthetized mice, respectively, $p = 7.4 \times 10^{-4}$, $t_{(51)} = -3.6$, Student's *t* test, $n = 9$ and 44 cells for awake and anesthetized mice, respectively), indicating that spontaneous activity was more mature in awake mice than in anesthetized mice.

A previous study (Yagishita et al., 2020) showed that SWRs in awake mice (i.e., less anesthetized condition) had higher event frequency and ripple power than in anesthetized mice. In the present study, ripple frequency was also higher in awake mice than in anesthetized mice (Fig. 6*E*, 135 ± 1.7 and 117 ± 0.37 Hz for awake and anesthetized mice, respectively, $p = 1.4 \times 10^{-49}$, $t_{(2121)} = 15.0$, Student's *t* test, $n = 241$ and 1882 SWRs for awake and anesthetized mice, respectively). Pre-SWR firing rates were higher in awake mice (Fig. 6*F*, 2.3 ± 1.6 and 0.37 ± 0.096 Hz for awake and anesthetized mice, respectively, $p = 0.010$, $t_{(51)} = 2.7$, Student's *t* test, $n = 9$ and 44 cells for awake and anesthetized mice, respectively), while during-SWR firing rates (1.9 ± 1.2 and 6.2 ± 0.93 Hz for awake and anesthetized mice, respectively) and post-SWR firing rates (0.23 ± 0.13 and 0.64 ± 0.21 Hz for awake and anesthetized mice, respectively) did not differ between the two conditions (Fig. 6*F*, $p = 0.054$ and 0.39, $t_{(51)} = -2.0$ and −0.87 for during and post-SWR periods, respectively; Student's *t* test, $n = 9$ and 44 cells for awake and anesthetized mice, respectively). At the subthreshold level, the FWHM values of depolarizations were smaller in awake mice (Fig. 6*G*, 34 ± 1.6 and 43 ± 0.47 ms for awake and anesthetized mice, respectively, $p = 2.1 \times 10^{-5}$, $t_{(3984)} = -4.3$, Student's *t* test, $n = 204$ and 3782 SWRs for awake and anesthetized mice, respectively). Although ΔVm_{pre} was not different between the two conditions (Fig. 6*H*, −0.076 ± 0.11 and −0.20 ± 0.028 mV for awake and anesthetized mice, respectively, $p = 0.30$, $t_{(4398)} = 1.0$, $n = 241$ and 4159 SWRs for awake and anesthetized mice, respectively), ΔVm_{during} (Fig. 6*I*, 3.6 ± 0.22 and 5.1 ± 0.053 mV for awake and anesthetized mice, respectively, $p = 1.4 \times 10^{-10}$, $t_{(4386)} = -6.4$, $n = 241$ and 4147 SWRs for awake and anesthetized mice, respectively) and ΔVm_{post} were smaller in awake mice (Fig. 6*J*, −2.0 ± 0.11 and −1.6 ± 0.032 for awake and anesthetized mice, respectively, $p = 4.8 \times 10^{-4}$, $t_{(4398)} = -3.5$, $n = 241$ and 4159 SWRs for awake and anesthetized mice, respectively). These results demonstrate that the SWR-related activity of pyramidal cells in awake mice had similar or more mature characteristics than those observed in anesthetized mice. Therefore, the immature neuronal activity observed in younger mice did not result from a low anesthetic dose.

Weak inhibitory and strong excitatory inputs in immature neurons

In the present study, we found that the activity of mature pyramidal cells was characterized by inhibition-dominant *V*m dynamics around SWRs. To directly examine the developmental changes in excitatory and inhibitory inputs, we voltage-clamped pyramidal cells at *V*m values of −70 and 10 mV and recorded

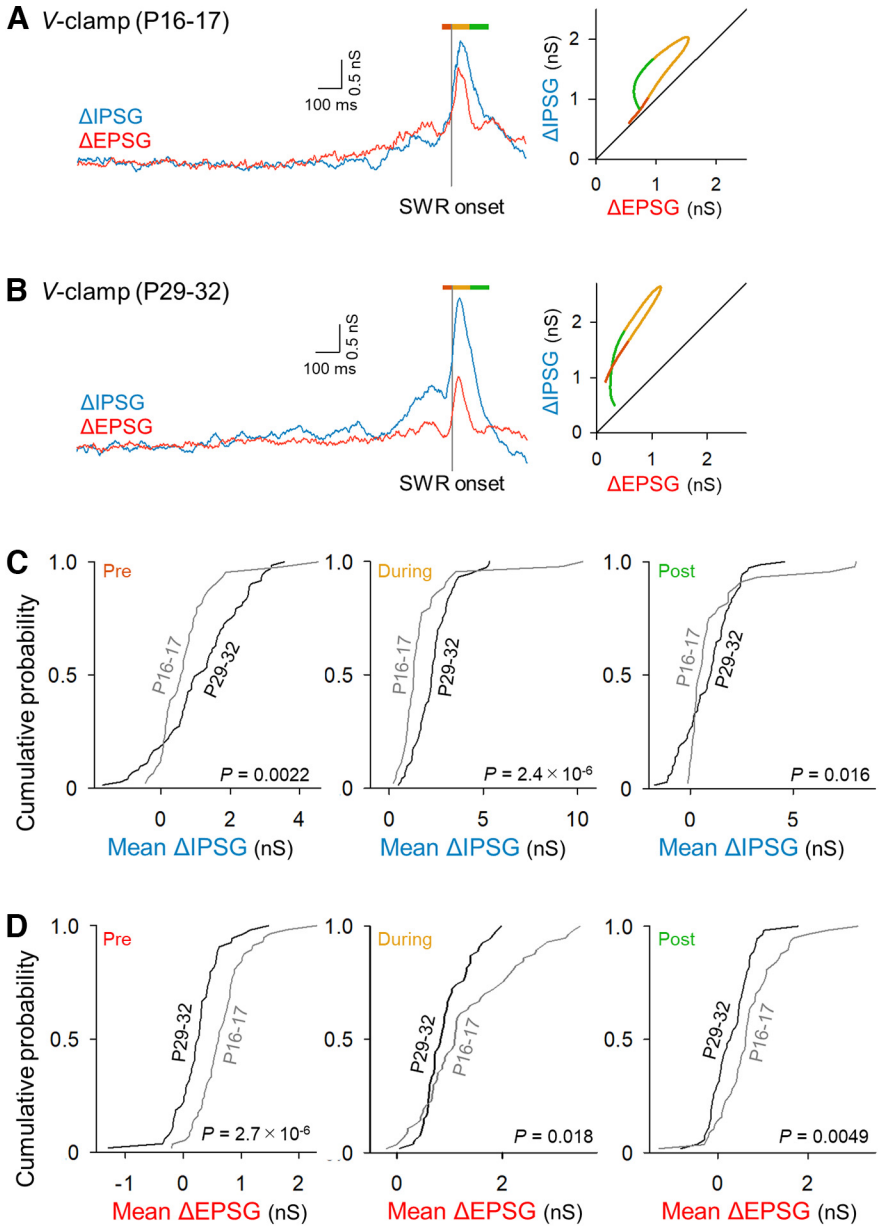

Figure 7. Developmental shifts toward inhibitory dominance of peri-SWR synaptic inputs. ***A***, Left, SWR onset-triggered average of the temporal evolution of 57 EPSGs (red) and 44 IPSGs (blue) recorded from 14 cells in 9 P16-P17 mice. Orange, yellow, and green bars above the traces represent pre-, during-, and post-SWR periods, respectively. Right, The temporal coevolution of EPSGs and IPSGs in the left traces during the period shown by the colored bars in the EPSG versus IPSG space. Pre-SWR EPSGs and pre-SWR IPSGs were balanced. ***B***, Same as in ***A***, but for 54 EPSGs and 62 IPSGs recorded from 7 cells in 7 mice on P29-P40. IPSGs increased in magnitude earlier than EPSGs. ***C***, Cumulative probability distributions of mean values of pre- (left), during- (middle), and post- (right) SWR IPSGs on P16-P17 (gray) and P29-P40 (black). Mean IPSGs on P16-P17 were smaller than those on P29-P40 throughout the peri-SWR period. $p = 0.0022$, 2.4×10^{-6}, and 0.016, $D = 0.34$, 0.49, and 0.29 for pre-, during, and post-SWR periods, respectively, two-sample Kolmogorov–Smirnov test. $n = 44$ and 73 SWR events in 14 and 7 cells from 9 and 7 mice for P16-P17 and P29-P40, respectively. ***D***, Same as in ***C***, but for EPSGs. Mean EPSGs on P16-P17 were larger than those on P29-P40 throughout the peri-SWR period. $p = 2.7 \times 10^{-6}$, 0.018, and 0.0049, $D = 0.48$, 0.28, and 0.32 for pre-, during, and post-SWR periods, respectively, two-sample Kolmogorov–Smirnov test. $n = 57$ and 54 SWR events in 10 and 7 cells from 7 and 7 mice for P16-P17 and P29-P40, respectively.

excitatory (EPSGs) and inhibitory postsynaptic conductances (IPSGs), respectively. The traces of EPSGs and IPSGs were averaged for 57 and 44 SWRs, respectively, in 14 cells from P16-P17 mice (Fig. 7*A*, 0.23 ± 0.0099 and 0.22 ± 0.013 nS for the mean EPSGs and IPSGs). We plotted the temporal evolution of the mean values of peri-SWR conductances in the EPSG versus IPSG space (Fig. 7*A*, right) and found that EPSGs and IPSGs were linearly balanced, with IPSGs drifting slightly above EPSGs. On the other hand, the mean traces of EPSGs and IPSGs for 54 and 62 SWRs, respectively, in 7 cells from P29-P32 mice (0.13 ± 0.0062 and 0.31 ± 0.016 nS for the mean EPSGs and IPSGs) demonstrate that IPSGs were dominant before SWR onset and remained greater than EPSGs throughout SWR events (Fig. 7*B*), which is consistent with previous reports (Gan et al., 2017; Noguchi et al., 2022). The mean values of IPSGs during pre- (0.73 ± 0.14 and 1.2 ± 0.14 nS for P16-P17 and P29-P32, respectively), during- (1.8 ± 0.29 and 2.3 ± 0.12 nS for P16-P17 and P29-P32, respectively), or post-SWR periods (1.1 ± 0.29 and 0.88 ± 0.14 nS for P16-P17 and P29-P32, respectively) were calculated for the P16-P17 and P29-P32 datasets (Fig. 7*C*). For all three periods, IPSGs were significantly smaller in P16-P17 mice than in P29-P32 mice (Fig. 7*C*, $p = 0.0022$, 2.4×10^{-6},

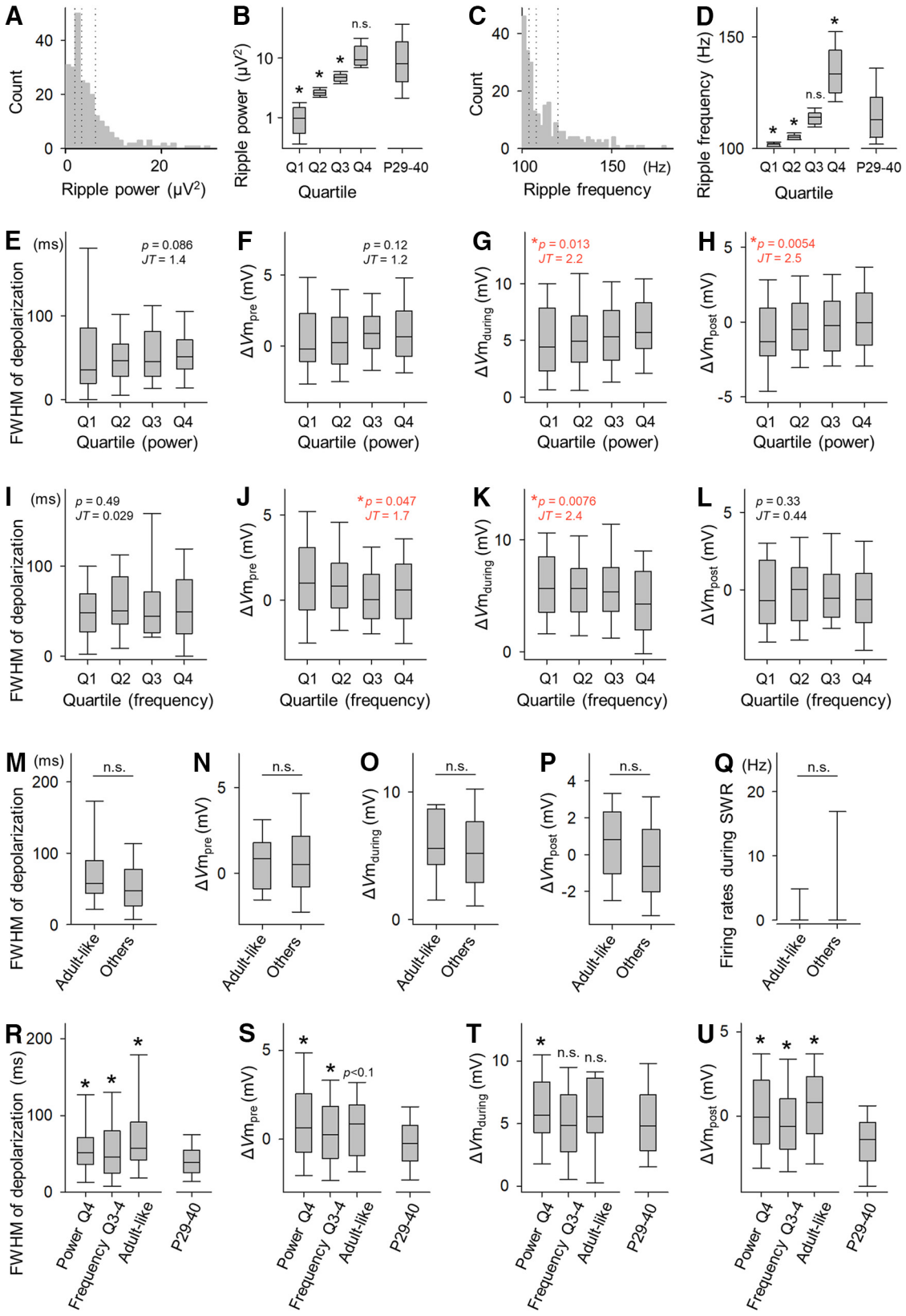

Figure 8. Neuronal activity on P16-P17 associated with adult-like SWRs is still immature. ***A***, The distribution of ripple power on P16-P17 was equally divided into quartiles. ***B***, Ripple power in each quartile was compared with that in P29-P40 mice. $p = 3.1 \times 10^{-7}$, 4.7×10^{-6}, 9.3×10^{-5}, and 0.19 for Q1, Q2, Q3, and Q4, respectively, $t_{(1940)} = -5.1$ (Q1) and -4.6 (Q2), $t_{(1941)} = -3.9$ (Q3), and -1.3 (Q4). Student's *t* test. $n = 61$ (Q1, Q2) and 62 (Q3, Q4) SWRs on P16-P17 and 1881 SWRs for P29-P40. ***C***, ***D***, Same as in ***A*** and ***B***, but for ripple frequency. $p = 1.8 \times 10^{-13}$, 2.0×10^{-8}, 0.13, and 2.6×10^{-21} for Q1, Q2, Q3, and Q4, respectively, $t_{(1940)} = -7.4$ (Q1) and -5.6 (Q2), $t_{(1941)} = -1.5$ (Q3), and 9.6 (Q4). ***E***, FWHM values of depolarizations on P16-P17 did not change according to ripple power. $p = 0.086$, $JT = 1.4$. $n = 61$ (Q1, Q2) and 62 (Q3, Q4) SWRs. ***F***, ΔVm_{pre} did not change with ripple power. $p = 0.12$, $JT = 1.2$. ***G***, ΔVm_{during} increased with ripple power. $p = 0.013$, $JT = 2.2$. ***H***, ΔVm_{post} increased with ripple power. $p = 0.0054$, $JT = 2.5$. ***I–L***, Same as in ***E–H***, but for the quartiles of ripple frequency. ΔVm_{pre} and ΔVm_{during} increased with ripple frequency. $p = 0.49$, 0.047, 0.0076, and 0.33, $JT = 0.029$, 1.7, 2.4, and 0.44 for ***I***, ***J***, ***K***, and ***L***, respectively. ***M***, FWHM values of depolarizations

and 0.016, $D = 0.34$, 0.49, and 0.29, respectively, for pre-, during-, and post-SWR periods, two-sample Kolmogorov–Smirnov test, $n = 44$ and 73 SWR events for P16-P17 and P29-P32, respectively). In contrast, EPSGs were significantly larger on P16-P17 than on P29-P32 (Fig. 7*D*, 0.66 ± 0.060 and 0.25 ± 0.057 nS for P16-P17 and P29-P32, respectively; $p = 2.7 \times 10^{-6}$, $D = 0.48$; Fig. 7*E*, 1.3 ± 0.12 and 0.92 ± 0.059, $p = 0.018$, $D = 0.28$; Fig. 7*F*, 0.68 ± 0.094 and 0.29 ± 0.062 nS, $p = 0.0049$, $D = 0.32$, $n = 57$ and 54 SWR events). These results suggest that increasing inhibitory inputs and decreasing excitatory inputs shape the mature SWR-associated *V*m dynamics.

Immature *V*m dynamics associated with adult-like SWRs in immature neurons

While ripple power and frequency are, on average, lower in immature mice than in adult mice, some SWRs on P16-P17 exhibited ripple power and frequency values comparable to those in adult mice. Therefore, we investigated whether the *V*m dynamics associated with these adult-like SWRs in P16-P17 mice were similar to those in adult mice. Specifically, we divided the distribution of ripple power and frequency in P16-P17 mice into quartiles (Fig. 8*A*,*C*; Q1-Q4) and analyzed the *V*m dynamics associated with each quartile. Ripple power in Q1 (1.0 ± 0.067 μV^2), Q2 (2.6 ± 0.045 μV^2), and Q3 (4.7 ± 0.10 μV^2) was lower than that in adult mice (16 ± 0.53 μV^2), but ripple power in Q4 (12 ± 0.77 μV^2) was comparable to that in adult mice (Fig. 8*B*, $p = 3.1 \times 10^{-7}$, 4.7×10^{-6}, 9.3×10^{-5}, and 0.19 for Q1, Q2, Q3, and Q4, respectively; $t_{(1940)} = -5.1$ (Q1) and -4.6 (Q2), $t_{(1941)} = -3.9$ (Q3), and -1.3 (Q4), Student's *t* test, $n = 61$ (Q1 and Q2) and 62 (Q3 and Q4) SWRs for P16-P17 and 1881 SWRs for P29-P40). Ripple frequencies in Q3 (114 ± 0.40 Hz) were comparable to those in adult mice (117 ± 0.36 Hz), whereas those in Q1 and Q2 (102 ± 0.11 Hz and 105 ± 0.16 Hz, respectively) and Q4 (136 ± 1.7 Hz) were lower and higher than those in adult mice (Fig. 8*D*, $p = 1.8 \times 10^{-13}$, 2.0×10^{-8}, 0.13, and 2.6×10^{-21} for Q1, Q2, Q3, and Q4, respectively, $t_{(1940)} = -7.4$ (Q1) and -5.6 (Q2), $t_{(1941)} = -1.5$ (Q3) and 9.6 (Q4), Student's *t* test; $n = 61$ (Q1 and Q2), 62 (Q3 and Q4) SWRs for P16-P17 and 1881 SWRs for P29-P40, respectively).

For each of the quartiles of ripple power, SWR-related *V*m dynamics were calculated and compared across quartiles (Fig. 8*E–H*). The FWHM of depolarization (75 ± 14, 56 ± 7.5, 58 ± 6.0, and 63 ± 6.8 ms, for Q1, Q2, Q3, and Q4, respectively) and ΔVm_{pre} (0.80 ± 0.42, 0.73 ± 0.38, 1.0 ± 0.26, and 1.0 ± 0.34 mV) did not vary by ripple power (Fig. 8*E*, $p = 0.086$, $JT = 1.4$, $n = 53$, 53, 55, and 54 SWRs for Q1, Q2, Q3, and Q4, respectively; Fig. 8*F*, $p = 0.12$, $JT = 1.2$, $n = 61$, 61, 62, and 62 SWRs for Q1, Q2, Q3, and Q4, respectively). Notably, ΔVm_{during} (5.0 ± 0.49, 5.2 ± 0.54, 5.6 ± 0.48, and 6.3 ± 0.49 mV for Q1, Q2, Q3, and Q4, respectively) and ΔVm_{post} (-0.85 ± 0.46, -0.040 ± 0.45, 0.22 ± 0.31, and 0.43 ± 0.38 mV) increased with ripple power (Fig. 8*G*, $p = 0.013$, $JT = 2.2$, $n = 58$, 58, 61, and 62 SWRs; Fig. 8*H*, $p = 0.0054$, $JT = 2.5$, $n = 61$, 61, 62, and 62 SWRs), suggesting that stronger ripples in P16-P17 mice were accompanied by less mature *V*m dynamics.

To investigate how synaptic inputs change with ripple power, the mean EPSGs and IPSGs during pre-SWR periods (0.66 ± 0.060 and 0.73 ± 0.14 nS, respectively), during-SWR periods (1.3 ± 0.12 and 1.8 ± 0.29 nS), and post-SWR periods (0.68 ± 0.094 and 1.1 ± 0.29 nS) were plotted against ripple power (10 ± 1.2 and 5.9 ± 0.92 μV^2). In line with the *V*m dynamics, neither pre-SWR EPSGs nor pre-SWR IPSGs showed a significant correlation with ripple power (Fig. 9*A*, $R = 0.19$ and 0.23, respectively, $p = 0.15$ and 0.13, *t* test of the correlation coefficient, $n = 57$ and 44 for EPSGs and IPSGs). On the other hand, during- and post-SWR EPSGs displayed significant positive correlations with ripple power (Fig. 9*B*,*C*, red, $R = 0.39$ and 0.39, respectively; $p = 0.0025$ and 0.0039 for Fig. 9*B*,*C*), while no significant correlation was observed between during- or post-SWR IPSGs and ripple power (Fig. 9*B*,*C*, blue, $R = 0.27$ and 0.27, respectively, $p = 0.081$ and 0.074 for Fig. 9*B*,*C*). The findings suggest that the increase in ripple power was associated with larger excitatory synaptic inputs in during- and post-SWRs period, which underlies the observed increase in ΔVm_{during} and ΔVm_{post}.

As the ripple frequency increased, no significant change was observed in the FWHM of depolarization (Fig. 8*I*, 56 ± 7.7, 67 ± 8.8, 69 ± 12, and 59 ± 7.5 ms for Q1, Q2, Q3, and Q4, respectively, $p = 0.49$, $JT = 0.029$ [Jonckheere Trend Test], $n = 55$, 52, 57, and 51) and ΔVm_{post} (Fig. 8*L*, -0.45 ± 0.43, -0.039 ± 0.34, 0.0039 ± 0.38, and -0.58 ± 0.39 mV, $p = 0.33$, $Z = 0.44$). On the other hand, ΔVm_{pre} (1.4 ± 0.40, 1.1 ± 0.34, 0.40 ± 0.31, and 0.68 ± 0.35 mV for Q1, Q2, Q3, and Q4, respectively) and ΔVm_{during} (6.2 ± 0.54, 5.8 ± 0.49, 5.8 ± 0.48, and 4.3 ± 0.47 mV) were larger for higher ripple frequencies (Fig. 8*J*, $p = 0.047$, $Z = 1.7$, $n = 61$, 61, 62, and 62 SWRs; Fig. 8*K*, $p = 0.0076$, $Z = 2.4$, $n = 60$, 60, 60, and 59 SWRs). No significant correlations were observed between ripple frequency (124 ± 3.1 and 115 ± 2.7 Hz for EPSGs and IPSGs, respectively) and EPSGs or IPSGs for all three periods (Fig. 9*D*, $R = -0.19$ and -0.051, $p = 0.15$ and 0.74; Fig. 9*E*, $R = -0.19$ and -0.12, $p = 0.15$ and 0.44; Fig. 9*F*, $R = -0.12$ and -0.088, $p = 0.37$ and 0.57, *t* test of the correlation coefficient, $n = 57$ and 44). The results suggest that higher ripple frequency could be associated with decreased E/I balance on SWR occurrence.

Next, we focused on adult-like SWRs, defined as SWRs in Q4 of ripple power and Q3 or Q4 of ripple frequency, and examined the *V*m dynamics. We found no significant differences in the four parameters examined between adult-like SWRs and other SWRs on P16-P17, that is, FWHM of depolarization (Fig. 8*M*, 71 ± 13 and 62 ± 4.8 ms, $n = 15$ and 200 SWRs for adult-like and other SWRs, respectively, $p = 0.62$, $t_{(213)} = 0.50$, Student's

←

were compared between adult-like SWRs (Q4 in ripple power and Q3-Q4 in ripple frequency) and other SWRs on P16-P17. No difference was observed. $p = 0.62$, $t_{(213)} = 0.50$, Student's *t* test. $n = 15$ and 200 SWRs for adult-like and other SWRs, respectively. ***N***, Same as in ***M***, but for ΔVm_{pre}. $p = 0.66$, $t_{244} = -0.43$. $n = 18$ and 228 SWRs for adult-like and other SWRs, respectively. ***O***, Same as in ***M***, but for ΔVm_{during}. $p = 0.93$, $t_{(237)} = 0.088$. $n = 18$ and 221 SWRs for adult-like and other SWRs, respectively. ***P***, Same as in ***M***, but for ΔVm_{post}. $p = 0.31$, $t_{(244)} = 1.0$. $n = 18$ and 228 SWRs for adult-like and other SWRs, respectively. ***Q***, Same as in ***M***, but for during-SWR firing rates. $p = 0.21$, $t_{244} = -1.2$. $n = 18$ and 228 SWRs for adult-like and other SWRs, respectively. ***R***, FWHM values of depolarizations were larger for SWRs in Q4 of ripple power, Q3-Q4 of ripple frequency and adult-like SWRs than for adult SWRs. Power Q4 versus P29-P40, $p = 7.8 \times 10^{-7}$, $t_{(3834)} = 4.9$, Student's *t* test. $n = 54$ and 3782 SWRs, respectively; Frequency Q3-Q4 versus P29-P40, $p = 2.6 \times 10^{-12}$, $t_{(3888)} = 7.0$. $n = 108$ and 3782 SWRs; Adult-like versus P29-P40, $p = 1.8 \times 10^{-4}$, $t_{(3795)} = 3.8$. $n = 15$ and 3782 SWRs. ***S***, ΔVm_{pre} was larger for SWR in Q4 of ripple power and Q3-Q4 of ripple frequency than for adult SWRs. Power Q4 versus P29-P40, $p = 2.5 \times 10^{-7}$, $t_{(4218)} = 5.2$. $n = 62$ and 4158 SWRs; Frequency Q3-Q4 versus P29-P40, $p = 1.1 \times 10^{-5}$, $t_{(4280)} = 4.4$. $n = 124$ and 4158 SWRs, Adult-like versus P29-P40, $p = 0.057$, $t_{(4174)} = 1.9$. $n = 18$ and 4158 SWRs. ***T***, ΔVm_{during} was larger for SWRs in Q4 of ripple power than for adult SWRs. Power Q4 versus P29-P40, $p = 0.0047$, $t_{(4219)} = 2.8$. $n = 62$ and 4159 SWRs; Frequency Q3-Q4 versus P29-P40, $p = 0.92$, $t_{(4276)} = -0.10$. $n = 119$ and 4159 SWRs, Adult-like versus P29-P40, $p = 0.51$, $t_{(4175)} = 0.66$, 18, and 4159 SWRs. ***U***, ΔVm_{post} was larger for SWRs in Q4 of ripple power, Q3-Q4 of ripple frequency and adult-like SWRs than for adult SWRs. Power Q4 versus P29-P40, $p = 2.9 \times 10^{-12}$, $t_{(4219)} = 7.0$. $n = 62$ and 4159 SWRs; Frequency Q3-Q4 versus P29-P40, $p = 2.5 \times 10^{-11}$, $t_{(4281)} = 6.7$. $n = 124$ and 4159 SWRs; Adult-like versus P29-P40, $p = 4.2 \times 10^{-5}$, $t_{(4175)} = 4.1$. $n = 18$ and 4159 SWRs.

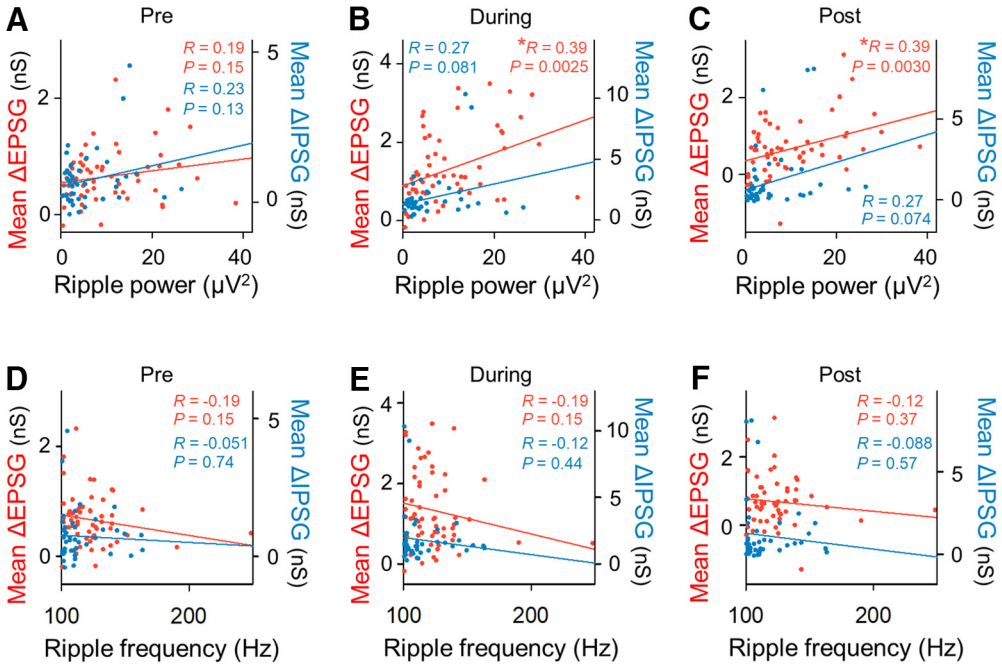

Figure 9. Relationships between synaptic inputs and ripple power or frequency on P16-P17. ***A***, Mean ΔEPSGs and ΔIPSGs during pre-SWR periods were plotted against ripple power. $R = 0.19$ and 0.23, $p = 0.15$ and 0.13. $n = 57$ and 44 for EPSGs and IPSGs, respectively, *t* test of the correlation coefficients. ***B***, Same as in ***A***, but for during-SWR periods. $R = 0.39$ and 0.27, $p = 0.0025$ and 0.081 for EPSGs and IPSGs, respectively. ***C***, Same as in ***A***, but for post-SWR periods. $R = 0.39$ and 0.27, $p = 0.0030$ and 0.074 for EPSGs and IPSGs, respectively. ***D***, Same as in ***A***, but for ripple frequency instead of ripple power. $R = -0.19$ and -0.051, $p = 0.15$ and 0.74 for EPSGs and IPSGs, respectively. ***E***, Same as in ***B***, but for ripple frequency instead of ripple power. $R = -0.19$ and -0.12, $p = 0.15$ and 0.44 for EPSGs and IPSGs, respectively. ***F***, Same as in ***C***, but for ripple frequency instead of ripple power. $R = -0.12$ and -0.088, $p = 0.37$ and 0.57 for EPSGs and IPSGs, respectively.

t test), ΔVm_{pre} (Fig. 8*N*, 0.62 ± 0.41 and 0.92 ± 0.19 mV, $n = 18$ and 228 SWRs, $p = 0.66$, $t_{(244)} = -0.43$), ΔVm_{during} (Fig. 8*O*, $p = 0.93$, $t_{(237)} = 0.088$, 5.6 ± 0.69 and 5.5 ± 0.27 mV, $n = 18$ and 221 SWRs), and ΔVm_{post} (Fig. 8*P*, 0.42 ± 0.53 and -0.32 ± 0.20, $n = 18$ and 228 SWRs, $p = 0.31$, $t_{(244)} = 1.0$). Firing rates during SWRs on P16-P17 did not differ between the two groups of SWRs (Fig. 8*Q*, 0.87 ± 0.60 and 3.6 ± 0.61 Hz, $n = 18$ and 228 SWRs for adult-like and other SWRs, respectively, $p = 0.21$, $t_{(244)} = -1.2$). These results suggest that immature pyramidal neurons show immature *Vm* dynamics even when adult-like SWRs with high ripple power and frequency occur.

Finally, we examined whether the *Vm* dynamics on P16-P17 with similar ripple power or frequency to those in the adult are immature in contrast to those in adult mice. The *Vm* dynamics accompanied by SWRs with high ripple power (Q4), frequency (Q3-Q4), or both (adult-like) were compared with those in adult mice. FWHM of depolarizations and ΔVm_{post} were larger for all three groups of SWRs on P16-P17 than those associated with adult SWRs (Fig. 8*R*, Power Q4 vs P29-P40, $p = 7.8 \times 10^{-7}$, $t_{(3834)} = 4.9$, Student's *t* test, $n = 54$ and 3782 SWRs, respectively; Frequency Q3-Q4 vs P29-P40, $p = 2.6 \times 10^{-12}$, $t_{(3888)} = 7.0$, $n = 108$ and 3782 SWRs; Adult-like vs P29-P40, $p = 1.8 \times 10^{-4}$, $t_{(3795)} = 3.8$, $n = 15$ and 3782 SWRs; Fig. 8*U*, Power Q4 vs P29-P40, $p = 2.5 \times 10^{-7}$, $t_{(4218)} = 5.2$, $n = 62$ and 4158 SWRs, respectively; Frequency Q3-Q4 vs P29-P40, $p = 1.1 \times 10^{-5}$, $t_{(4280)} = 4.4$, $n = 124$ and 4158 SWRs, Adult-like vs P29-P40, $p = 0.057$, $t_{(4174)} = 1.9$, $n = 18$ and 4158 SWRs). ΔVm_{pre} was larger for SWRs on P16-P17 with high ripple power or frequency than for adult SWRs (Fig. 8*S*, Power Q4 vs P29-P40, $p = 2.5 \times 10^{-7}$, $t_{(4218)} = 5.2$, $n = 62$ and 4158 SWRs, respectively; Frequency Q3-Q4 vs P29-P40, $p = 1.1 \times 10^{-5}$, $t_{(4280)} = 4.4$, $n = 124$ and 4158 SWRs, Adult-like vs P29-P40, $p = 0.057$, $t_{(4174)} = 1.9$, $n = 18$ and 4158 SWRs). ΔVm_{during} was larger for SWRs on P16-P17 with high ripple power than for adult SWRs (Fig. 8*T*, Power Q4 vs P29-P40, $p = 0.0047$, $t_{(4219)} = 2.8$, $n = 62$ and 4159 SWRs; Frequency Q3-Q4 vs P29-P40, $p = 0.92$, $t_{(4276)} = -0.10$, $n = 119$ and 4159 SWRs, Adult-like vs P29-P40, $p = 0.51$, $t_{(4175)} = 0.66$, 18 and 4159 SWRs). These results indicate that the *Vm* dynamics on P16-P17, even associated with adult-like SWRs, are still immature, except for the similar ΔVm_{during} between SWRs on P16-P17 with high ripple frequency and adult SWRs, suggesting that during-SWR inhibitory dynamics are mainly related to ripple frequencies on P16-P17.

Discussion

We discovered that hippocampal CA1 pyramidal cells at the beginning of SWR emergence exhibited high excitability with loose temporal specificity in both suprathreshold and subthreshold activity. We also demonstrated gradual maturation of peri-SWR inhibition, which is thought to temporally control the spike times of pyramidal cells during SWRs in mature mice (English et al., 2014; Stark et al., 2015; Noguchi et al., 2022). The present study provides the first observation of *in vivo Vm* dynamics of CA1 pyramidal neurons during postnatal development and proposes the neural mechanisms underlying less organized SWR-associated spike patterns in immature mice and their maturation throughout the third and fourth postnatal weeks (Farooq and Dragoi, 2019) at the single-cell *Vm* level.

Frequent but temporally disorganized spikes do not represent substantial information, as is the case in unorganized spike sequences in immature SWRs during postnatal development (Farooq and Dragoi, 2019). These loosely timed spikes may be because of broader depolarizations during SWRs in the

immature hippocampus. In addition, we found that pre- and post-SWR inhibition, which emerges with age, narrowed the width of SWR-related depolarizations. This narrow depolarization may regulate the temporal window to allow pyramidal cells to fire spikes. Our voltage-clamp data demonstrated smaller inhibitory inputs and larger excitatory inputs to pyramidal cells around SWRs in immature mice, which may underlie the age-dependent changes in peri-SWR *V*m dynamics. The smaller IPSGs are attributable to the immaturity of $GABA_A$-receptor-mediated inhibition (Cohen et al., 2000; Groen et al., 2014) and presynaptic interneurons (Le Magueresse et al., 2011). Among subtypes of CA1 interneurons, we believe that parvalbumin (PV)-positive basket cells mediate the growing inhibition based on their maturation in anatomic, intrinsic, and synaptic properties during the third and fourth postnatal weeks (Du et al., 1996; Doischer et al., 2008; Le Magueresse et al., 2011). This view is supported by the pivotal contribution of PV-positive basket cells to the SWR-associated activity of pyramidal cells in adult mice (Lapray et al., 2012; Varga et al., 2014; Gan et al., 2017; Geiller et al., 2020). We also showed an age-dependent decrease in EPSGs, which appears inconsistent with the increase in excitatory synaptic transmission from CA3 to CA1 pyramidal cells throughout the developmental period (Hsia et al., 1998). One possibility is that maturation of the inhibitory control of pyramidal cells in the CA1 and CA3 subregions (Romo-Parra et al., 2008; Sauer and Bartos, 2011; Groen et al., 2014) and dominant inhibition during adult SWRs (Hájos et al., 2013; Hulse et al., 2016; Gan et al., 2017; Kajikawa et al., 2022) led the increased IPSGs to override the increased EPSGs.

Consistent with a previous report (Buhl and Buzsáki, 2005), we detected high-frequency oscillations at the end of the second postnatal week, but their frequencies on P14-P15 were low and cannot be considered mature SWRs. This may be attributable to anesthesia in our experimental conditions (Ylinen et al., 1995). The increases in SWR event frequency and power are consistent with previous studies in freely moving rats (Buhl and Buzsáki, 2005; Farooq and Dragoi, 2019). We also observed an increase in ripple frequency during the fourth postnatal week. This result is in line with a previous study that reported stable frequencies of ~140 Hz from P12 to P20, although our study observed lower frequencies because of the use of urethane anesthesia (Fig. 6*E*). Given that the ripple frequency is ~200 Hz in freely behaving adult mice (Csicsvari and Dupret, 2014; Roumis and Frank, 2015), it is likely that SWRs with higher ripple frequencies might increase after the third postnatal week in freely behaving animals, but further investigation is necessary to confirm this possibility. In contrast to the previous study showing longer SWR events in older rats (Farooq and Dragoi, 2019), in our study, the duration of SWRs did not change, at least during the early developmental period of interest. Considering that long-duration SWRs are linked to learning and memory (Fernández-Ruiz et al., 2019), we might have failed to capture learning-dependent changes in SWR durations in adult animals. In addition to the characteristics of individual SWRs, we also reported an age-dependent increase in successive SWRs (Davidson et al., 2009; Yamamoto and Tonegawa, 2017), which are defined herein as two or more adjacent SWRs with IEIs of 250 ms. This result is consistent with that of a previous work (Farooq and Dragoi, 2019), which reported an increase in ripple doublets during development as a function of age. The entorhinal cortex is thought to trigger successive SWRs in quiet awake conditions, while it is dispensable during slow-wave sleep for successive SWRs (Yamamoto and Tonegawa, 2017; Oliva et al., 2018). Since our recordings were obtained from urethane-anesthetized mice, which exhibit slow-wave-sleep-like activity (Pagliardini et al., 2013; González-Rueda et al., 2018), the observed developmental increase in successive SWRs may largely reflect changes in the inputs from the CA3 subregion. Successive SWRs have been linked to extended replays of long paths (Davidson et al., 2009). The developmental increase in successive SWRs may correspond to an increasing need for complex information processes, which are behaviorally accompanied by increased spatial exploration.

We found that CA1 pyramidal neurons on P16-P17 show higher excitability (Chen et al., 2005), which was characterized by higher firing rates and more depolarized mean *V*m, than neurons in adult mice. Previous *in vitro* studies have reported that the maturation of excitable membrane properties occurs during the first two postnatal weeks and that the resting *V*m of CA1 pyramidal cells becomes more hyperpolarized (Spigelman et al., 1992; Giglio and Storm, 2014), which seems incompatible with our data. The discrepancy may derive from the difference between *in vivo* and *in vitro* conditions; the anatomic structure is less preserved in slice preparations. We assume that higher *V*m on P16-P17 results from the immaturity of dendritic tonic inhibition (Cohen et al., 2000; Caraiscos et al., 2004; Ramos et al., 2004; Glykys and Mody, 2006; Groen et al., 2014) and that this effect is weakened in *in vitro* slices because of the loss of synaptic connections from inhibitory interneurons to pyramidal cells. We also reported larger ISIs and fewer burst firings on P16-P17 (Ranck, 1973; Harris et al., 2001). Spike bursts are usually initiated by synchronous excitatory inputs (Magee and Carruth, 1999). Indeed, more synchronous excitatory inputs from the CA3 subregion (Tyzio et al., 2003) and the entorhinal cortex (Donato et al., 2017) occurred in more mature dendrites (Groen et al., 2014).

On P16-P17, *V*m dynamics remained immature even when accompanied by SWRs with high ripple power, frequency, or both. It has been suggested that, in adult mice, IPSGs rather than EPSGs scale with SWR amplitudes (Gan et al., 2017), leading to the assumption that adult-like ripple power is associated with greater hyperpolarization (i.e., more mature *V*m dynamics). However, we found that stronger SWRs were accompanied by larger excitatory inputs, resulting in more depolarized values of ΔVm_{during} and ΔVm_{post}. This discrepancy may be explained by the immaturity of the local inhibitory circuits in the CA1 subregion, which might have failed to provide sufficient feedback inhibition to pyramidal cells, leading to larger during and post-SWR depolarizations. In contrast, a higher ripple frequency was associated with greater hyperpolarization (i.e., more mature ΔVm_{pre} and ΔVm_{during}). Moreover, ΔVm_{during} on P16-P17 with high ripple frequency was similar to that in the adult. These results are convincing given that higher frequency oscillations are paced by the activity of PV-positive basket cells at higher firing rates (Stark et al., 2014). Although no significant correlation was observed between synaptic inputs and ripple frequency (Fig. 9*D–F*), the E/I balance might be dominated by inhibition when higher-frequency SWRs occur. The absence of a relationship between ΔVm_{post} and ripple frequency could be explained by the immaturity of local feedback inhibition within the CA1.

It is notable that pre-SWR IPSGs were balanced with pre-SWR EPSGs, whereas post-SWR IPSGs already exceeded post-SWR EPSGs on P16-P17, characterizing the difference in synaptic activity between pre- and post-SWR periods at the beginning of the third postnatal week. CA1 pyramidal cells receive feedback inhibition during and post-SWRs, particularly from PV-positive basket cells (Stark et al., 2014; Buzsáki, 2015),

which shape during and post-SWR hyperpolarization along with feedforward inhibition (Valero et al., 2015; Hulse et al., 2016). On the other hand, pre-SWR hyperpolarization reflects preceding feedforward inhibition via CA1 interneurons that is driven by excitatory inputs from the CA2/3 subregions (Pouille et al., 2009; Bhatia et al., 2019; Noguchi et al., 2022). Thus, feedforward and feedback inhibition to CA1 pyramidal cells differs in developmental processes. Because the synaptic connectivity from CA3 pyramidal cells to CA1 pyramidal cells continues to increase after the third postnatal week (Spigelman et al., 1992; Hsia et al., 1998), it is probable that the synaptic contacts from CA2/CA3 pyramidal cells to CA1 interneurons also develop during the third and fourth postnatal weeks.

In conclusion, our study describes SWR-associated *V*m dynamics *in vivo* and provides possible mechanisms underlying the disorganized spike sequences of CA1 pyramidal cells in immature mice. The developmental time course of the maturation of *V*m dynamics, characterized by growing inhibition and its regulation of the time window for spikes, is compatible with the maturation of the sequential structure of replays (Farooq and Dragoi, 2019) and episodic memory (Travaglia et al., 2016). Several studies have suggested that instructive signals from the upstream network of the entorhinal cortex contribute to hippocampal replays (Schlesiger et al., 2015; Donato et al., 2017). In addition to this extrahippocampal mechanism, our results propose the concurrently maturing intrinsic and local-circuit properties in the hippocampus as factors for the developmental emergence of temporally organized activity during SWRs (Farooq and Dragoi, 2019).

References

Bhatia A, Moza S, Bhalla US (2019) Precise excitation-inhibition balance controls gain and timing in the hippocampus. Elife 8:e43415.

Buhl DL, Buzsáki G (2005) Developmental emergence of hippocampal fast-field 'ripple' oscillations in the behaving rat pups. Neuroscience 134:1423–1430.

Buzsáki G (2015) Hippocampal sharp wave-ripple: a cognitive biomarker for episodic memory and planning. Hippocampus 25:1073–1188.

Caraiscos VB, Elliott EM, You-Ten KE, Cheng VY, Belelli D, Newell JG, Jackson MF, Lambert JJ, Rosahl TW, Wafford KA, MacDonald JF, Orser BA (2004) Tonic inhibition in mouse hippocampal CA1 pyramidal neurons is mediated by α5 subunit-containing γ-aminobutyric acid type A receptors. Proc Natl Acad Sci USA 101:3662–3667.

Chen S, Yue C, Yaari Y (2005) A transitional period of Ca^{2+}-dependent spike afterdepolarization and bursting in developing rat CA1 pyramidal cells. J Physiol 567:79–93.

Cohen AS, Lin DD, Coulter DA (2000) Protracted postnatal development of inhibitory synaptic transmission in rat hippocampal area CA1 neurons. J Neurophysiol 84:2465–2476.

Csicsvari J, Dupret D (2014) Sharp wave/ripple network oscillations and learning-associated hippocampal maps. Philos Trans R Soc Lond B Biol Sci 369:20120528.

Davidson TJ, Kloosterman F, Wilson MA (2009) Hippocampal replay of extended experience. Neuron 63:497–507.

Doischer D, Hosp JA, Yanagawa Y, Obata K, Jonas P, Vida I, Bartos M (2008) Postnatal differentiation of basket cells from slow to fast signaling devices. J Neurosci 28:12956–12968.

Donato F, Jacobsen RI, Moser MB, Moser EI (2017) Stellate cells drive maturation of the entorhinal-hippocampal circuit. Science 355:eaai8178.

Du J, Zhang L, Weiser M, Rudy B, McBain CJ (1996) Developmental expression and functional characterization of the potassium-channel subunit Kv3.1b in parvalbumin-containing interneurons of the rat hippocampus. J Neurosci 16:506–518.

Ekstrom AD, Ranganath C (2018) Space, time, and episodic memory: the hippocampus is all over the cognitive map. Hippocampus 28:680–687.

English DF, Peyrache A, Stark E, Roux L, Vallentin D, Long MA, Buzsáki G (2014) Excitation and inhibition compete to control spiking during hippocampal ripples: intracellular study in behaving mice. J Neurosci 34:16509–16517.

Farooq U, Dragoi G (2019) Emergence of preconfigured and plastic time-compressed sequences in early postnatal development. Science 363:168–173.

Fernández-Ruiz A, Oliva A, Fermino de Oliveira E, Rocha-Almeida F, Tingley D, Buzsáki G (2019) Long-duration hippocampal sharp wave ripples improve memory. Science 364:1082–1086.

Foster DJ (2017) Replay comes of age. Annu Rev Neurosci 40:581–602.

Funayama K, Hagura N, Ban H, Ikegaya Y (2016) Functional organization of flash-induced V1 offline reactivation. J Neurosci 36:11727–11738.

Funayama K, Minamisawa G, Matsumoto N, Ban H, Chan AW, Matsuki N, Murphy TH, Ikegaya Y (2015) Neocortical rebound depolarization enhances visual perception. PLoS Biol 13:e1002231.

Gan J, Weng SM, Pernía-Andrade AJ, Csicsvari J, Jonas P (2017) Phase-locked inhibition, but not excitation, underlies hippocampal ripple oscillations in awake mice in vivo. Neuron 93:308–314.

Geiller T, Vancura B, Terada S, Troullinou E, Chavlis S, Tsagkatakis G, Tsakalides P, Ócsai K, Poirazi P, Rózsa BJ, Losonczy A (2020) Large-scale 3D two-photon imaging of molecularly identified CA1 interneuron dynamics in behaving mice. Neuron 108:968–983.e9.

Giglio AM, Storm JF (2014) Postnatal development of temporal integration, spike timing and spike threshold regulation by a dendrotoxin-sensitive K^+ current in rat CA1 hippocampal cells. Eur J Neurosci 39:12–23.

Girardeau G, Zugaro M (2011) Hippocampal ripples and memory consolidation. Curr Opin Neurobiol 21:452–459.

Glykys J, Mody I (2006) Hippocampal network hyperactivity after selective reduction of tonic inhibition in GABAA receptor α5 subunit–deficient mice. J Neurophysiol 95:2796–2807.

González-Rueda A, Pedrosa V, Feord RC, Clopath C, Paulsen O (2018) Activity-dependent downscaling of subthreshold synaptic inputs during slow-wave-sleep-like activity in vivo. Neuron 97:1244–1252.e5.

Groen MR, Paulsen O, Pérez-Garci E, Nevian T, Wortel J, Dekker MP, Mansvelder HD, van Ooyen A, Meredith RM (2014) Development of dendritic tonic GABAergic inhibition regulates excitability and plasticity in CA1 pyramidal neurons. J Neurophysiol 112:287–299.

Hájos N, Karlócai MR, Németh B, Ulbert I, Monyer H, Szabó G, Erdélyi F, Freund TF, Gulyás AI (2013) Input-output features of anatomically identified CA3 neurons during hippocampal sharp wave/ripple oscillation *in vitro*. J Neurosci 33:11677–11691.

Harris KD, Hirase H, Leinekugel X, Henze DA, Buzsáki G (2001) Temporal interaction between single spikes and complex spike bursts in hippocampal pyramidal cells. Neuron 32:141–149.

Hsia AY, Malenka RC, Nicoll RA (1998) Development of excitatory circuitry in the hippocampus. J Neurophysiol 79:2013–2024.

Hulse BK, Moreaux LC, Lubenov EV, Siapas AG (2016) Membrane potential dynamics of CA1 pyramidal neurons during hippocampal ripples in awake mice. Neuron 89:800–813.

Ishikawa D, Matsumoto N, Sakaguchi T, Matsuki N, Ikegaya Y (2014) Operant conditioning of synaptic and spiking activity patterns in single hippocampal neurons. J Neurosci 34:5044–5053.

Kajikawa K, Hulse BK, Siapas AG, Lubenov EV (2022) UP-DOWN states and ripples differentially modulate membrane potential dynamics across DG, CA3, and CA1 in awake mice. Elife 11:e69596.

Kuga N, Sasaki T, Takahara Y, Matsuki N, Ikegaya Y (2011) Large-scale calcium waves traveling through astrocytic networks *in vivo*. J Neurosci 31:2607–2614.

Lapray D, Lasztoczi B, Lagler M, Viney TJ, Katona L, Valenti O, Hartwich K, Borhegyi Z, Somogyi P, Klausberger T (2012) Behavior-dependent specialization of identified hippocampal interneurons. Nat Neurosci 15:1265–1271.

Le Magueresse C, Alfonso J, Khodosevich K, Arroyo Martín ÁA, Bark C, Monyer H (2011) 'Small axonless neurons': postnatally generated neocortical interneurons with delayed functional maturation. J Neurosci 31:16731–16747.

Le Magueresse C, Monyer H (2013) GABAergic interneurons shape the functional maturation of the cortex. Neuron 77:388–405.

Lee AK, Wilson MA (2002) Memory of sequential experience in the hippocampus during slow wave sleep. Neuron 36:1183–1194.

Magee JC, Carruth M (1999) Dendritic voltage-gated ion channels regulate the action potential firing mode of hippocampal CA1 pyramidal neurons. J Neurophysiol 82:1895–1901.

Matsumoto N, Okamoto K, Takagi Y, Ikegaya Y (2016) 3-Hz subthreshold oscillations of CA2 neurons in vivo. Hippocampus 26:1570–1578.

Mizunuma M, Norimoto H, Tao K, Egawa T, Hanaoka K, Sakaguchi T, Hioki H, Kaneko T, Yamaguchi S, Nagano T, Matsuki N, Ikegaya Y (2014) Unbalanced excitability underlies offline reactivation of behaviorally activated neurons. Nat Neurosci 17:503–505.

Mizuseki K, Buzsáki G (2013) Preconfigured, skewed distribution of firing rates in the hippocampus and entorhinal cortex. Cell Rep 4:1010–1021.

Noguchi A, Huszár R, Morikawa S, Buzsáki G, Ikegaya Y (2022) Inhibition allocates spikes during hippocampal ripples. Nat Commun 13:1280.

O'Keefe J, Nadel L (1979) Précis of O'Keefe and Nadel's The hippocampus as a cognitive map. Behav Brain Sci 2:487–494.

Oliva A, Fernández-Ruiz A, Fermino de Oliveira E, Buzsáki G (2018) Origin of gamma frequency power during hippocampal sharp-wave ripples. Cell Rep 25:1693–1700.e4.

Pagliardini S, Gosgnach S, Dickson CT (2013) Spontaneous sleep-like brain state alternations and breathing characteristics in urethane anesthetized mice. PLoS One 8:e70411.

Pouille F, Marin-Burgin A, Adesnik H, Atallah BV, Scanziani M (2009) Input normalization by global feedforward inhibition expands cortical dynamic range. Nat Neurosci 12:1577–1585.

Ramos B, Lopez-Tellez JF, Vela J, Baglietto-Vargas D, del Rio JC, Ruano D, Gutierrez A, Vitorica J (2004) Expression of α5 GABAA receptor subunit in developing rat hippocampus. Brain Res Dev Brain Res 151:87–98.

Ranck JB (1973) Studies on single neurons in dorsal hippocampal formation and septum in unrestrained rats: I. Behavioral correlates and firing repertoires. Exp Neurol 41:462–531.

Romo-Parra H, Treviño M, Heinemann U, Gutiérrez R (2008) GABA actions in hippocampal area CA3 during postnatal development: differential shift from depolarizing to hyperpolarizing in somatic and dendritic compartments. J Neurophysiol 99:1523–1534.

Roumis DK, Frank LM (2015) Hippocampal sharp-wave ripples in waking and sleeping states. Curr Opin Neurobiol 35:6–12.

Sakaguchi T, Ishikawa D, Nomura H, Matsuki N, Ikegaya Y (2012) Normal learning ability of mice with a surgically exposed hippocampus. Neuroreport 23:457–461.

Sauer JF, Bartos M (2011) Postnatal differentiation of cortical interneuron signalling. Eur J Neurosci 34:1687–1696.

Schlesiger MI, Cannova CC, Boublil BL, Hales JB, Mankin EA, Brandon MP, Leutgeb JK, Leibold C, Leutgeb S (2015) The medial entorhinal cortex is necessary for temporal organization of hippocampal neuronal activity. Nat Neurosci 18:1123–1132.

Spigelman I, Zhang L, Carlen PL (1992) Patch-clamp study of postnatal development of CA1 neurons in rat hippocampal slices: membrane excitability and K^+ currents. J Neurophysiol 68:55–69.

Stark E, Roux L, Eichler R, Senzai Y, Royer S, Buzsáki G (2014) Pyramidal cell-interneuron interactions underlie hippocampal ripple oscillations. Neuron 83:467–480.

Stark E, Roux L, Eichler R, Buzsáki G (2015) Local generation of multineuronal spike sequences in the hippocampal CA1 region. Proc Natl Acad Sci USA 112:10521–10526.

Travaglia A, Bisaz R, Sweet ES, Blitzer RD, Alberini CM (2016) Infantile amnesia reflects a developmental critical period for hippocampal learning. Nat Neurosci 19:1225–1233.

Tyzio R, Ivanov A, Bernard C, Holmes GL, Ben-Ari Y, Khazipov R (2003) Membrane potential of CA3 hippocampal pyramidal cells during postnatal development. J Neurophysiol 90:2964–2972.

Valero M, Cid E, Averkin RG, Aguilar J, Sanchez-Aguilera A, Viney TJ, Gomez-Dominguez D, Bellistri E, de la Prida LM (2015) Determinants of different deep and superficial CA1 pyramidal cell dynamics during sharp-wave ripples. Nat Neurosci 18:1281–1290.

Varga C, Oijala M, Lish J, Szabo GG, Bezaire M, Marchionni I, Golshani P, Soltesz I (2014) Functional fission of parvalbumin interneuron classes during fast network events. Elife 3:e04006.

Yagishita H, Nishimura Y, Noguchi A, Shikano Y, Ikegaya Y, Sasaki T (2020) Urethane anesthesia suppresses hippocampal subthreshold activity and neuronal synchronization. Brain Res 1749:147137.

Yamamoto J, Tonegawa S (2017) Direct medial entorhinal cortex input to hippocampal CA1 is crucial for extended quiet awake replay. Neuron 96:217–227.e4.

Ylinen A, Soltész I, Bragin A, Penttonen M, Sik A, Buzsáki G (1995) Intracellular correlates of hippocampal theta rhythm in identified pyramidal cells, granule cells, and basket cells. Hippocampus 5:78–90.